

CONTINUOUS SNOW WATER EQUIVALENT MEASUREMENTS WITH ULTRA-  
WIDEBAND RADAR: *TOWARDS A NEW GENERATION OF REAL-TIME*  
*AUTOMATED SNOW SENSOR ARRAYS*

by

Mark Edward Robertson

A thesis

submitted in partial fulfillment

of the requirements for the degree of

Master of Science in Geophysics

Boise State University

December 2016

© 2016

Mark Edward Robertson

**ALL RIGHTS RESERVED**

BOISE STATE UNIVERSITY GRADUATE COLLEGE

**DEFENSE COMMITTEE AND FINAL READING APPROVALS**

of the thesis submitted by

Mark Edward Robertson

Thesis Title: Continuous Snow Water Equivalent Measurements with Ultra-Wideband Radar: Towards a New Generation of Real-Time Automated Snow Sensor Arrays

Date of Final Oral Examination: 21 October, 2016

The following individuals read and discussed the thesis submitted by student Mark Edward Robertson, and they evaluated his presentation and response to questions during the final oral examination. They found that the student passed the final oral examination.

Hans-Peter Marshall, Ph.D. Chair, Supervisory Committee

John Bradford, Ph.D. Member, Supervisory Committee

James P. McNamara, Ph.D. Member, Supervisory Committee

The final reading approval of the thesis was granted by Hans-Peter Marshall, Ph.D., Chair of the Supervisory Committee. The thesis was approved by the Graduate College.

## ACKNOWLEDGEMENTS

This work was supported by Flat Earth, Inc., which generously provided radar hardware, software support and the vision for a network of radar sites for measuring SWE. Partial funding was also provided from a NASA New Investigator Program grant (#NNX10AO02G), and a NASA EPSCoR grant (#NNX10AN30A).

The National Resources Conservation Service in Idaho, particularly Ron Abramovich and Ivan Geroy, were encouraging and flexible with their support for co-located radar measurements at the Bogus Basin, Banner Summit and Vienna Mine SNOTEL sites.

Thanks are also owed to the many who helped in the field, including Jesse Dean, Joel Gongora, Andrew Hedrick and Scott Havens. Particular thanks is owed to Sam Evans and Chago Rodriguez, who were indispensable with many snow pit measurements. Special thanks goes to Andrew Karlson, who did all of that, and more, with a positive attitude that is infectious.

HP, at some point along the way we agreed that my work would be complete when we had a day in the snow together in which I didn't roll a snowmobile or destroy equipment. At the risk of reminding you, that day has not yet come, but hopefully we can let it slide. Thank you for so much, not least of which has been your patience, guidance and the opportunity in the first place. You are a gift to all your students.

To my parents: while I often pretend that I walk on my own, your steadiness, support and love, given freely for my entire life, have caught me more times than you know. If I can give to Annika and Blake what you have given me, I will have succeeded.

And to Bob and Kathy: thank you for accepting me with such grace into your family, and for caring for all of us in so many ways. I cannot imagine being where we are without you.

Megan, I am forever grateful for your little lie on Valentine's Day all those years ago. You continue to show me the way and make the journey fun. Your strength is inspiring. Finally, Annika and Blake, both of you are my blue sky.

## ABSTRACT

Snow accounts for the majority of precipitation in many areas of the Western United States, and accurate measurements of the amount of water contained in the snowpack, known as snow water equivalent (SWE), are therefore important for water resource managers. The National Resources Conservation Service Snow Telemetry (SNOTEL) sites are the current standard remote measurement of SWE, with approximately 800 sites across the Western United States. Measurements at these sites are made by snow pillows, which weigh the overburden pressure of a snowpack, and are relatively expensive to install and maintain. Spring runoff is modeled using a 30-year average of SNOTEL SWE values, and recent years are increasingly diverging from the historical record as climate change impacts both the timing and amount of runoff. Additional measurements of in-situ SWE would increase model performance, but the current technology is several decades old and has limited range for site expansion. Radar has been proven to effectively measure SWE since the 1970s, but has not been developed as an operational sensor because the technology has been expensive and the data processing has not been developed for real-time applications necessary for remote sites.

This study applies a novel automatic processing algorithm, which inputs raw radar data and outputs SWE values available for transmission, to newly available hardware. The combination of automatic processing and new, high-resolution hardware allows radar to continuously measure SWE at remote sites, which have the potential to make radar the next generation of SWE sensor technology.

The accuracy of the radar was first determined by a series of focused, 1-2m radar profiles over subsequently excavated manual snow pits, with accuracy of 7% in SWE compared to manual measurements. A network of eight radars was deployed at remote sites in Idaho, Montana, and Colorado. Three of the eight remotely deployed radars were located at sites with independent SWE or precipitation measurements: Bogus Basin SNOTEL, Banner Summit SNOTEL and Garden Mountain weather station. Automatically processed radar SWE values are compared to the traditional snow pillow SWE values at the Bogus Basin and Banner Summit SNOTEL sites, and to a precipitation gauge at the Garden Mountain weather station. Radar-derived SWE values were highly correlated with SNOTEL SWE values, as well as with the precipitation gauge values of water equivalent. The combination of new hardware and an automatic processing algorithm has proven that radar can be an effective sensor for remotely measuring SWE in a range of alpine snowpacks.

## TABLE OF CONTENTS

ACKNOWLEDGEMENTS .....	iv
ABSTRACT .....	vi
LIST OF TABLES .....	x
LIST OF FIGURES .....	xi
LIST OF ABBREVIATIONS .....	xvii
CHAPTER ONE: CONTINUOUS SNOW WATER EQUIVALENT MEASUREMENTS WITH ULTRA-WIDEBAND RADAR: TOWARDS A NEW GENERATION OF REAL-TIME AUTOMATED SNOW SENSOR ARRAYS .....	1
1 Introduction .....	1
1.1 Importance of Snow Measurements for Water Resources .....	1
1.2 Snow Water Equivalent Measurements .....	2
1.3 History of Radar for Snow Measurements .....	6
2 Ground Penetrating Radar Theory and Methods .....	12
2.1 Theory .....	12
2.2 Spectral Shift Approach for Estimating Liquid Water .....	14
2.3 Approximations .....	16
2.4 Methods .....	17
3 Continuous SWE Measurement with a Low Power Radar System .....	20
3.1 Hardware .....	22
3.2 Autonomous Radar Measurement Network .....	23

3.3 Signal Processing .....	28
3.4 Real-Time Algorithm.....	35
4 Results.....	41
4.1 Comparison to Manual Snow Pits.....	41
4.2 Tower Mounted Sites.....	47
5 Discussion.....	64
6 Recommendations for Future Work.....	67
7 Conclusion .....	69
REFERENCES .....	72
APPENDIX.....	79
Real Time Code .....	79

## LIST OF TABLES

Table 1.1	Overview of Eight Tower-Based Radar Installations .....	24
-----------	---	----

## LIST OF FIGURES

Figure 1.	Radar velocity as a function of snow density for dry snow.....	7
Figure 2.	Radar velocity as a function of snow density and LWC. Since radar velocity in water is much less than in snow, accurate estimates of LWC are necessary to accurately measure SWE. Inset shows resulting SWE values for a theoretical range of snow density and LWC values in a 2m snow pack.....	10
Figure 3.	Following the complex permittivity of water, the complex permittivity of wet snow exhibits frequency-dependent behavior. All plots are a function of frequency. Subplot (a) shows the frequency dependent behavior of $\epsilon_s''$ for both actual $\epsilon_s''$ (solid lines) and the consequence of the assumption of linear fit to $\epsilon_s''$ (dashed lines) for LWC values from 0-4% (colored lines). The results of the linear fit assumption are shown for LWC in Subplot (b), and the radar velocity in wet snow in Subplot (c). Subplot (d) shows the resulting SWE underestimate that is generated by the linear fit assumption for 0-4% LWC for a theoretical 2m snowpack with a density of $400\text{kg m}^{-3}$ ..	17
Figure 4.	Values of the complex permittivity of water as a function of frequency..	19
Figure 5.	Instantaneous frequency (Taner et al., 1979) of a trace from February 1, 2016, at the Banner Summit SNOTEL. Black line shows the instantaneous frequency calculated Equation (34), and the blue dashed line shows the instantaneous frequency using the mean of a two sample window of the instantaneous phase.....	20
Figure 6.	Locations of eight tower-based radar locations. ....	23
Figure 7.	Banner Summit SNOTEL site, approximately 0.5 km west of Banner Summit, Idaho. The foreground tower holds two arm mounts: the upper arm holds the NRCS ultrasonic depth sensor, and the lower arm supports the radar antenna, with orange frame and white enclosure facing downward that covers the bowtie antenna. The radar ground footprint is approximately $12\text{m}^2$ , most of which overlaps the SNOTEL snow pillow directly underneath, although the bottom of the tower is also in the field of view. The desire to have the radar and SNOTEL pillow footprints overlapping to the greatest possible extent resulted in a non-ideal antenna mounting configuration, in which the base of the tower was within radar	

footprint. This caused difficulty in selecting the ground surface reflection.  
 ..... 27

- Figure 8. A temperature correction to the effective sample rate was created from field data and applied to all other data sets. Subplot (a) shows field data from four days at the Banner Summit SNOTEL in which the snow surface (blue) and ground surface (orange) are visible. It was a calm period at the SNOTEL site and the ultrasonic depth sensor showed no change in snow depth, ambient temperature was sub-freezing and the radar showed no significant LWC. Despite this, both the snow surface and ground surface vary significantly in time each afternoon, and also with respect to each other. Subplot (b) shows the varying number of samples between the snow and ground surfaces (blue line) and the temperature recorded on the radar chip (orange line). Assuming that the distance between the snow and ground surfaces is not, in fact, changing in time and the radar velocity is also not changing ( $LWC=0$ ), the sample interval required to meet this assumption is calculated. This estimated sample interval is modeled as a quadratic function of temperature. The radar signal is then resampled to the corrected sample interval, as shown in (b), and then the surfaces are seen to no longer vary in time in the radargram ..... 30
- Figure 9. Two traces taken several hours apart on January 28, 2015 at the Bogus SNOTEL. Subplot (a) shows the difference in mean trace amplitude between the two traces, and Subplot (b) details the differences in the direct wave for the same two traces. Subplot (c) shows the traces with the peak in the direct wave set to one..... 31
- Figure 10. The same two traces in Fig. 9 are shown with the trace set to time zero at the peak in the direct wave, with the full trace in Subplot (a) and detail of the first 70 samples in Subplot (b). ..... 32
- Figure 11. Raw and processed signals for the Garden Mountain site for the period January 3 – March 5, 2016, showing a more coherent ground reflection after trace processing. Significant daily-scale variations in two-way travel time to the ground reflection, which appears between 20 and 25ns, are corrected so that changes greater than 1-3 samples in the ground reflection correspond to changes in SWE ..... 33
- Figure 12. Focused radar profile prior to manual snow pit excavation at the same location. In this representative profile the radar antenna was moved vertically by hand from approximately 0-90cm above the snow surface. For a single trace the snow and ground surface reflections are difficult to distinguish, but with antenna movement they separate from constant system noise. Snow and ground reflections are picked by hand over 10-20 traces, from which the two-way travel time is calculated..... 34

Figure 13.	Background color is the absolute envelope showing the ground surface reflection at 400-420 samples at a section of data from the Garden Mountain site, March, 2016. The initial ground picks, $r_i$ , are shown in yellow, and can be seen to have a $\pm 3$ sample variation that is a remnant of the temperature correction to the sample interval. When the signal has undergone more attenuation around trace 7170 and the ground surface reflection becomes less clear $r_i$ also spikes significantly to other peaks. The final ground picks, $r_g$ , shown in red and the median of the previous 30 values of $r_i$ , smooth both the single-trace and significant spike variability. The result of the 30 trace window median can also be seen in the slight lag in $r_g$ responding to the dip in ground surface reflection around trace 7090. ..... 40
Figure 14.	Using snow pit measurements of depth, radar calculations of density are compared with pit density over a series of 15 pits. Error bars on the manual snow pit density are $\pm 9\%$ . For 12 of the 15 pits the radar density was within $\pm 9\%$ of the manual density ..... 43
Figure 15.	Using snow pit measurements of depth and radar measurements of density, radar calculations of SWE are compared with pit SWE for the same series of 15 pits as in Fig. 14. Error bars for the manual SWE are $\pm 9\%$ multiplied by the pit depth. For 12 of the 15 pits the radar SWE was within the uncertainty of the manual measurements. Red squares shown the consequences of an arbitrarily chosen density, in this case $320\text{kg m}^{-3}$ , applied to the independent depth measurements. For this arbitrary density the number of radar estimates of SWE that fall within the manual SWE uncertainly drop from 12 to 5 ..... 44
Figure 16.	Radar-derived LWC values for 12 hour daytime periods at the 2014 Bogus Ridge Site are shown as boxplots for days when manual snow pit measurements were also collected. Snow Fork values, as the mean of all values taken at 10cm intervals, are shown as green circles. Although the correlation between median radar-derived LWC and mean Snow Fork values is low, high Snow Fork values can be explained from those measurements being collected last in the snow pit, giving the pack time to drain to the pit face. Radar-derived LWC are physically reasonable and the presence of water is corroborated by Snow Fork measurements..... 45
Figure 17.	Change in depth and SWE as a result of a theoretical snow pack with 20ns two-way travel time and $400\text{ kg m}^{-3}$ density as a function of LWC..... 46
Figure 18.	Radar (black) and SNOTEL (blue) SWE values, as well as the difference in SWE (green) for the Bogus Basin SNOTEL for the period November 1 <sup>st</sup> , 2015 – March 1 <sup>st</sup> , 2016. The radar-derived SWE output was from the automatic algorithm with three updated ground surface reflection windows on December 2, 2015, January 6, 2016 (coincident with lowering the

antenna arm) and January 15, 2016. Several data gaps are present in this data set: the loss from mid-December to early January was the result of power loss; the loss in early February was the result of a firmware failure; the loss in late February was intentional removal of the radar system for testing..... 50

- Figure 19. Percent error between radar-derived and Bogus Basin SNOTEL SWE values for the period of observation is shown in Subplot (a). The higher percent differences through mid-December correspond to relatively low differences in actual SWE amounts during the early season snow pack. Subplot (b) shows the total percent error of  $-16 \pm 12\%$  and absolute percent error of  $16 \pm 8\%$  for the period of observation..... 51
  
- Figure 20. Correlation between radar-derived and SNOTEL SWE measurements at the Bogus Basin SNOTEL site, which have a  $R^2$  value of 0.98. Despite relatively high percent error between radar and SNOTEL SWE measurements, the two are highly correlated..... 51
  
- Figure 21. Bogus Basin SNOTEL temperature and radar-derived LWC. Temperature is color scaled, and the black line shows the daily mean temperature. Though the non-zero radar-derived LWC values are physical reasonable in isolation, and generally correspond with periods of above-freezing temperatures, there are large periods of time in which significant above-freezing temperatures do not result in non-zero LWC values ..... 53
  
- Figure 22. There is no correlation between radar-derived LWC and temperature at the Bogus Basin SNOTEL site for the observed period ..... 53
  
- Figure 23. Radar (black) and SNOTEL (blue) SWE values, as well as the difference in SWE (green) for the Banner Summit SNOTEL for the period January 12 – April 12, 2016, as processed by the automatic algorithm. The algorithm was updated at three points during the processing: February 9, February 15 and March 4, 2016. No filtering or other changes were applied to the algorithm outputs beyond the adjusted ground windows on those dates. The several sub-daily spikes in SWE, both positive and negative, correspond to places in which the automatic algorithm erroneously picked the ground surface, but soon recovered to the proper reflection target. The drop in radar SWE from February 14-16 is also erroneous, and represents a period in which the ground reflection was not obvious. After April 1, the ground surface also becomes difficult to pick and radar SWE values are increasingly variable. Note also that after the initial accumulation in mid-January the radar shows a strong positive bias in SWE. One possible explanation of this, which was also observed at the Bogus Basin SNOTEL, is that bridging of the SNOTEL pillow resulted in under-measurement of SWE. Radar-derived SWE is also stable on a daily scale, which suggests the high bias as compared to the SNOTEL values is

	not caused by daily spikes in LWC content, at least until mean daily temperatures remain below freezing prior to early April.....	55
Figure 24.	Percent error for radar-derived SWE as compared to Banner Summit SNOTEL values by date (a), as well as percent error of $-9 \pm 5\%$ and absolute percent error for the full period of $9 \pm 5\%$ (b).....	56
Figure 25.	Correlation between radar-derived and SNOTEL SWE measurements at the Banner Summit site, which have a $R^2$ value of 0.97 .....	56
Figure 26.	Banner Summit SNOTEL temperature and radar-derived LWC. Temperature is color scaled, and the black line shows the daily mean temperature. LWC values respond well to above freezing temperatures on a daily-to-weekly scale. The issue of daily-scale zero values of LWC during periods of relatively warm temperatures, as observed at the Bogus Basin SNOTEL site, are not repeated at the Banner Summit SNOTEL site .....	57
Figure 27.	Correlation between Banner Summit SNOTEL temperature and radar-derived LWC has a $R^2$ value of 0.45 .....	58
Figure 28.	Precipitation gauge water equivalent (blue) and radar-derived SWE (black) for the Garden Mountain site. Also shown is a factor of 1.85 applied to the precipitation gauge value (green), which matches well with radar-derived SWE for the period with shaded background, January 7-30, 2016, when temperatures were cold and precipitation would have fallen as snow. Precipitation gauge measurements begin on November 1 <sup>st</sup> , and the radar was installed on December 16 <sup>th</sup> , 2015. The gap in precipitation gauge measurement corresponds to power loss at the gauge. Radar-derived SWE measurements are the output of the automatic algorithm, with no specific or updated ground surface window .....	60
Figure 29.	Correlation of precipitation gauge water equivalent and radar-derived SWE for the Garden Mountain site for periods of coincident measurement, with a $R^2$ value of 0.94 .....	61
Figure 30.	Correlation between radar-derived SWE and mean precipitation gauge at Garden Mountain, for the 100 hour period beginning January 3, 2016. Subplot (a) shows water equivalent from the radar (black), mean precipitation gauge (solid blue) and best fit factor of two applied to the mean precipitation (dashed blue), with values zeroed to the beginning of the period. The 7cm SWE event was highly correlated with $R^2$ value of 0.97.....	62
Figure 31.	Garden Mountain temperature and radar-derived LWC. As with other tower-mounted sites there was not an independent measurement of LWC	

to compare to radar-derived values. However, the LWC signal generally appears to follow expected trends based on temperature data, especially the relatively spike in LWC follow a warm period in early February, and again in late February. Although daily temperature values drop below freezing between these warming events, the drop to zero LWC values between would seem to indicate an artifact of the processing, especially given non-zero LWC values in January ..... 63

Figure 32. Correlation of temperature and LWC content at the Garden Mountain site, with a  $R^2$  value of 0.42 ..... 64

## LIST OF ABBREVIATIONS

BSU	Boise State University
FMCW	Frequency-modulated continuous-wave
GPR	Ground Penetrating Radar
GPS	Global Positioning System
LWC	Liquid Water Content
NRCS	National Resources Conservation Service
SNOTEL	Snow Telemetry
SNR	Signal-to-noise ratio
SWE	Snow Water Equivalent
TDC	Thesis and Dissertation Coordinator
upGPR	Upward-looking Ground Penetrating Radar

CHAPTER ONE: CONTINUOUS SNOW WATER EQUIVALENT MEASUREMENTS  
WITH ULTRA-WIDEBAND RADAR: TOWARDS A NEW GENERATION OF  
REAL-TIME AUTOMATED SNOW SENSOR ARRAYS

**Introduction**

1.1 Importance of Snow Measurements for Water Resources

The majority of available surface water in the Western United States arrives as snow during the winter accumulation period (Serreze et al., 1999). The seasonal snowpack in these areas controls both the timing of peak stream flow and the total water availability for hydropower, municipal and industrial uses. Significant increases in population in the Western United States in the last several decades have put additional demand on water resources, while changing climate patterns have generally led to earlier peak stream flow and drought in many areas (Bales et al., 2006). Operational hydrologic models of stream flow require inputs of the amount of water stored in the snowpack, and since both the density and depth of a snow pack are variable (e.g. Blöschl, 1999; Bormann et al., 2013), the amount of water contained in a snowpack is reported as the density multiplied by the depth, or snow water equivalent (SWE). The standard remote measurement of SWE in the Western United States is the network of United States Department of Agricultural Natural Resources Conservation Service (NRCS) Snow Telemetry (SNOTEL) sites. While these sites have been the standard remote measurement of SWE since the 1960's, additional inputs of remote SWE and improved forecasting performance require new technology and an expanded network of sites.

This study combines a novel automatic processing algorithm with newly available ground penetrating radar (GPR) hardware to demonstrate that radar can accurately measure SWE at remote sites. Radar has been used to measure snow properties for several decades, but has not been applied operationally over full winter seasons, mainly because the processing of raw radar data into transmittable SWE values has required user input and interaction, and because commercially available radar requires too much power. The application of automatic radar processing accomplished in this study, applied to a new low power radar system, demonstrates that radar can be deployed operationally. This study also characterizes the accuracy of the radar in SWE measurements using manual methods and comparisons to existing SNOTEL pillows.

### 1.2 Snow Water Equivalent Measurements

Standardized point measurements of SWE in the Western United States began with NRCS snow course measurements. These manual *in-situ* snow courses are bi-weekly or monthly measurements of SWE at selected sites which were chosen to correlate well with spring runoff (U.S. Soil Conservation Service, 1972), and which eventually peaked at approximately 2000 sites in the late 1970's. Beginning in the early 1960's, the NRCS began installing automated measurement Snow Telemetry (SNOTEL) sites which standardized the timing, quality and location of automated snow measurements, as a replacement for the labor intensive monthly snow course manual observation sites. The SNOTEL sites consist of a bladder of antifreeze solution laying at ground level which measures the pressure caused by the snow overburden, via a manometer column, and have become the standard remote measurement of SWE in the Western United States. SNOTEL sites telemeter hourly measurements of SWE, as well as

snow depth as measured by an ultrasonic depth sensor, often accompanied by temperature and wind speed data. These sites require a flat ground surface of approximately 20m<sup>2</sup> for the antifreeze pillow to be installed, an outbuilding for the manometer reading and consistent maintenance of the antifreeze pillow. The current SNOTEL network consists of approximately 859 sites, with the locations bounded by the requirement for a level ground surface and maintenance needs of the antifreeze pillow. SNOTEL locations are generally not representative of the larger basin area (Molotch and Bales, 2005). Additionally, these sites were chosen to maintain a strong correlation with streamflow, and therefore were often chosen in places that maintain significant snowcover well into the spring melt season, rather than locations that are representative of the larger region. However, even this large network of sites is still far too sparse to spatially interpolate a distributed SWE estimate, as the correlation length for bulk snow properties is on the order of 50-200m (Deems et al., 2006; Trujillo et al., 2009). Accurately modeling the amount and timing of snowmelt is critical for water resource managers. Currently, the NRCS uses statistical relationships with stream flow based on the most recent 30 years on record to model spring stream flow (Day, 1985).

However, climate change is resulting in patterns of winter accumulation and spring melt that are not well represented in the historical record. In the Western United States the last several decades have been shown to depart from previous years through decreasing winter precipitation (Graves and Chang, 2007) and warmer temperatures (Loukas et al., 2002; Hamlet and Lettenmaier, 2007), including declines in available water in the Colorado, Columbia and Sierra river basins (Barnett et al., 2008) and reductions in annual flow in the Pacific Northwest (Luce and Holden, 2009). Statistical

models of streamflow, such as are used by the NRCS, suffer from increasing uncertainty (Pagano et al., 2004) as snowmelt-dominated systems experience new and unique accumulation and melt patterns (Milly et al., 2008; Mote, 2003; Stewart et al., 2004; Mote et al., 2005; Maurer, 2007). Runoff modeling approaches that incorporate additional model scenarios and employ more physically based approaches, such as energy balance models, have shown improvements over purely statistical methods (Franz et al., 2008; Garen and Marks, 2005; Georgakakos et al., 2004), but are still challenged by sparse SWE observations. All modeling approaches gain performance with additional, spatially distributed, inputs of SWE (Franz et al., 2008). Additional *in-situ* measurements of SWE beyond what is currently available from the SNOTEL network would improve estimates of the timing and amount of stream flow in the Western United States, although the current standard technology and site requirements make this impractical.

Snow depth is, at first glance, an attractive method of measuring SWE, as the measurements, either by hand or by relatively inexpensive and reliable instruments such as an ultrasonic depth sensor, are both easier and faster to acquire than density measurements. However, snow depth has much greater spatial variability than SWE (e.g. Elder et al., 1998; Mizukami and Perica, 2008; Sturm et al., 2010), and is variable temporally on hourly, seasonal, and inter-annual scales (e.g. Meløysund et al., 2007; Svomova, 2011). Snow density models have been employed to bridge the gap between snow depth and SWE, from empirical (e.g. Sturm et al., 1995) to energy-balance model (Marks et al., 1999) and are used in combination with snow depth operationally in some parts of Europe (e.g. Jonas et al., 2009). These density models must be locally calibrated, and although they work well in smaller research basins, they struggle when applied at the

regional scale. While combining the relatively inexpensive snow depth measurements with a model of density to achieve SWE has benefits, it is possible to measure SWE more directly, which has a history dating back several decades in the Western United States.

Several new technologies for remotely measuring SWE have become available in recent years, including load cell (Johnson et al., 2015), gamma ray (Offenbacher and Colbeck, 1991; Wright et al., 2011) and GPS signals (e.g. Larson et al., 2009; McCreight et al., 2014). Load cells operate with the same principle as the snow pillow used by the SNOTEL sites, by weighing the overburden of snow. Rather than recording the pressure in a fluid-filled pillow, a series of plates are supported by load cells. These sensors require a similarly-sized planar area on the ground surface, excavated so that the plate surfaces are level with the ground. SWE measurements made with load cells are affected by similar processes as pillows: bridging that may lead to under-measurement caused by significant mid-pack layers distributing weight, and increased heat flux through the plates at the ground surface that may cause some melt at the plate/snow interface (e.g. Beaumont, 1965). Gamma ray sensors are a passive measurement of the background gamma radiation of the soil. The emitted gamma radiation is attenuated by an overlying snowpack over a relatively large area, 50-100m<sup>2</sup>. These sensors are highly sensitive to soil moisture, and have increased accuracy in relatively shallow snowpacks with sub-25cm SWE. GPS methods use the signal-to-noise ratio (SNR) of multipath reflections from the ground recorded by high precision GPS receivers. As snow increases on the ground both the amplitude and frequency of the SNR changes as a function of snow depth. This method is sensitive to liquid water in the snow and requires density information to obtain SWE. The GPS approach has the advantage of a large areal average

(~100x100m), but requires an expensive survey-grade GPS unit, and unobstructed sky view to the south. Airborne and satellite SWE techniques exist (e.g. Dietz et al., 2012; Pulliainen, 2006), but suffer from large uncertainties in mountainous areas caused by variable terrain, large pixel size, and sensitivity to snow microstructure, and are not yet operational for water supply forecasts. Lidar is also used to measure snow depth, and basin-scale aerial lidar is currently being used operationally (Painter et al., 2016). Energy-balance models of snow density are combined with spatially dense depth measurements to estimate SWE. The benefit of this approach is very small pixel size estimates of SWE; however, the basin-scale airborne operations are prohibitively expensive for some water resource managers, and little work has been done to quantify the uncertainty in SWE estimates with independent methods.

### 1.3 History of Radar for Snow Measurements

Radar has been used to accurately measure snow properties, including depth and SWE, in research applications for several decades (e.g. Ellerbruch and Boyne, 1980; Gubler and Hiller, 1984; Annan et al., 1994; Marshall et al., 2005; Marshall and Koh, 2008; Bradford et al., 2009), using both frequency-modulated continuous wave (FMCW) and impulse radars. In the radar approach to measuring SWE, an electromagnetic signal is transmitted into the snowpack, and differences in electromagnetic properties between air, ice, water and the ground result in reflections of the signal at the snow and ground interfaces, as well as at major snow layer boundaries (e.g. Jol, 2009). Empirical relationships have been established between the electrical permittivity of snow and the density and liquid water content (Tiuri et al., 1984).

In the impulse radar approach, a voltage impulse is transmitted, and the received signal in the time domain is digitally recorded. This signal is used to estimate the elapsed time between the transmitted signal and reflections from the snow/air and snow/ground interfaces. The time difference between these two arrivals is used to estimate a bulk snowpack two-way travel time. When combined with an estimate of snow depth, the two-way travel time can be used to calculate the radar velocity. In the case of dry snow, in which the radar signal travels through only air and ice, the velocity is a function only of snow density, and there are well-established relationships that exist between radar velocity and snow density (Tiuri et al., 1984) (Fig. 1).

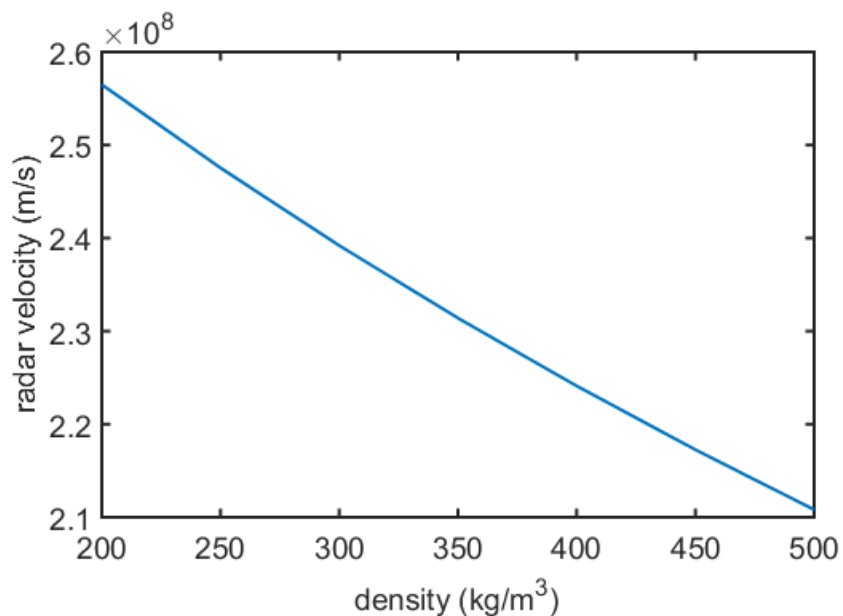


**Figure 1. Radar velocity as a function of snow density for dry snow.**

The majority of applications of radar for snow measurements have focused on the dry snow case, in which no liquid water is present. Impulse radar has proven to be a useful tool for measuring SWE in seasonal snowpacks (e.g. Lundberg and Thunehed,

2000; Marchand et al., 2003), and has seen the most use, as there are many impulse radar systems at the appropriate frequencies that are commercially available.

In the FMCW approach, a signal in which the frequency varies linearly in time is transmitted over a period which is much longer than the two-way travel time to the farthest reflector of interest, and the difference in frequency between transmitted and received signals can be converted to a travel time (e.g. Marshall and Koh, 2008). FMCW hardware is attractive in that it is possible to obtain a large bandwidth (>2GHz) and subsequent high depth resolution relatively inexpensively. FMCW radars have been used to measure snow properties for several decades (e.g. Ellerbruch et al., 1977; Marshall and Koh, 2008).

Upward-looking radar systems have been used to continuously measure snow properties, including FMCW (Gubler and Hiller, 1984) and impulse (e.g. Schmid et al., 2014; Heilig et al., 2015). Upward-looking ground penetrating radar (upGPR) has seen much development recently and has been used to measure snow properties and SWE over full winter seasons (e.g. Schmid et al., 2014; Heilig et al., 2009; Heilig et al., 2015; Okorn et al., 2014). These systems are installed in an enclosed case at ground level, with the antenna pointing upward, and are subsequently buried as snow accumulates. Most of the successful experiments used linear actuators to physically move the antennas up and down a distance of 10's of cm, which allows noise to more efficiently be separated from snow-related reflections.

Upward-looking systems are beneficial in places where the tower and arm necessary to mount a downward-looking antenna is difficult or impractical, although they typically employ additional equipment to determine snow depth, such as ultrasonic depth

sensor or laser range finder. Since the base of the snowpack is typically drier than the surface layers, especially once melt has started in late winter and early spring, upward-looking radars identify a clear reflection from the base of the diurnal wetting front (Schmid et al., 2014). Liquid water content (LWC) values are estimated, using a mixing model approach, to estimate volumes of air, ice and liquid water (Heilig et al., 2009; Heilig et al., 2015) and upGPR-derived LWC has been used to estimate snowpack holding capacity, evaluate water values in snowpack modeling, and has been also been compared with outflow measured by lysimeters (Heilig et al., 2015). One difficulty of the upward-looking approach is that the last relevant reflection, the snow/air interface at the top of the pack, typically has a much weaker dielectric contrast than the snow/ground interface at the base of the pack, necessitating a motor to move the antenna during measurements to separate constant system noise with the relatively weak surface signal.

Several recent studies have moved beyond dry snow only and have applied radar measurements in cases of wet snow. Once there is liquid water present in the snowpack becomes a three component system, and since the radar velocity in dry snow is much faster than radar velocity in water ( $v_{\text{dry snow}}/v_{\text{water}} \approx 7$ ) (Fig. 2), a reasonable LWC estimate must be made or SWE is overestimated (Lundberg and Thunehed, 2000).

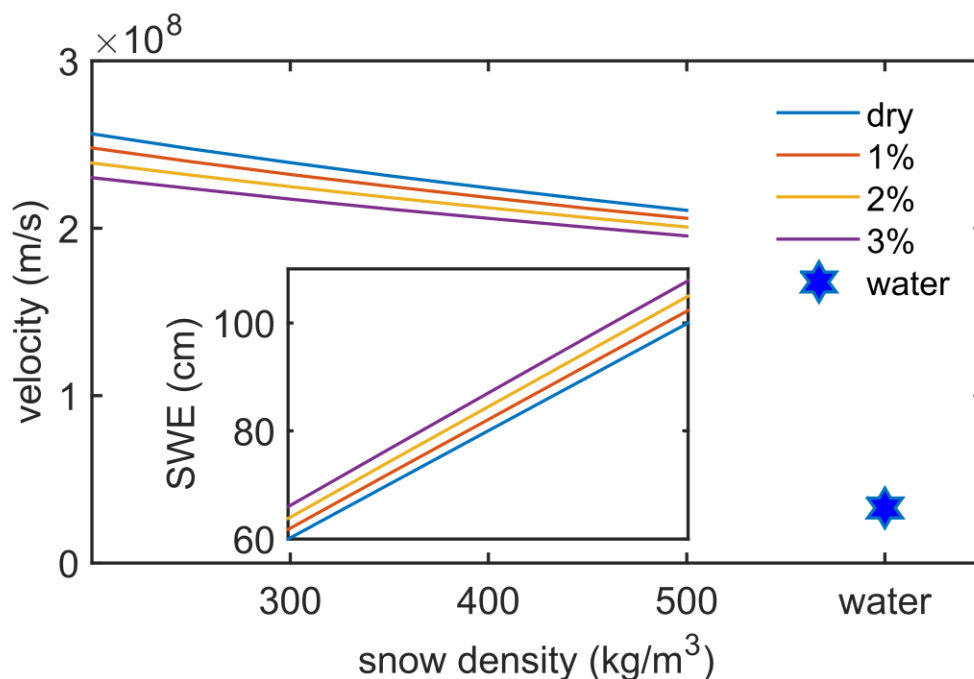


**Figure 2.** Radar velocity as a function of snow density and LWC. Since radar velocity in water is much less than in snow, accurate estimates of LWC are necessary to accurately measure SWE. Inset shows resulting SWE values for a theoretical range of snow density and LWC values in a 2m snow pack.

The established petrophysical relationships that relate the complex permittivity to snow density have also been extended to LWC (Tiuri et al., 1984). Following that radar velocity in snow is a function of snow density and LWC, another approach is to use known snow depth to calculate the effective velocity and then use a mixing model approach to estimate LWC (Mitterer et al., 2011; Schmid et al., 2014), and this has been applied to continuous upGPR measurements (Heilig et al., 2015).

The spectral shift method is yet another approach to estimating LWC values (Bradford et al., 2009). Liquid water in wet snow causes frequency-dependent attenuation of the radar signal, and the spectral shift method takes advantage of the frequency downshift between the radar signal reflections at the snow surface and ground surface after traveling through the wet snow to estimate LWC. Bradford et al. (2009) applied the spectral shift method for SWE estimates over small transects in alpine snowpacks.

Independent measurements of LWC are challenging, however, and generally require destructive sampling in manually excavated snow pits. The Finnish Snow Fork (Sihvola and Tiuri, 1986) is a hand-held instrument that transmits a 0.5-1.5 GHz signal through a small waveguide, and subsequently measures the complex permittivity of the snow based on the frequency-dependent attenuation due to liquid water. The Denoth meter is handheld capacitance probe, which, when combined with a separate manual density measurement, can be used to estimate the complex permittivity of a 13cm<sup>2</sup> area around the plate insertion. The accuracy of both instruments is approximately  $\pm 0.5\%$  LWC by volume (Sihvola and Tiuri, 1986; Fierz and Fohn, 1994), and a manually excavated snow pit is necessary to employ both the Denoth and Snow Fork, which limits direct, independent evaluation of radar LWC estimates. Tipping bucket lysimeters that measure outflow have also been compared to radar-derived LWC (Heilig et al., 2015).

This study applies the spectral shift approach for measuring LWC, developed by Bradford et al. (2009), to both focused profiles over evaluation snow pits, as well as the continuous tower-mounted measurements. For the series of snow pits that contained measurable LWC, radar-derived values are compared to those measured by the Finnish Snow Fork.

## 2 Ground Penetrating Radar Theory and Methods

### 2.1 Theory

First, the plane wave solution for a propagating electric field is described, from which the radar signal and spectral shift method can be described and applied. Maxwell's equations in matter are:

$$\nabla \cdot \mathbf{E} = \frac{\rho_f}{\varepsilon} \quad (1)$$

$$\nabla \cdot \mathbf{B} = 0 \quad (2)$$

$$\nabla \times \mathbf{E} = -\frac{\partial \mathbf{B}}{\partial t} \quad (3)$$

$$\nabla \times \mathbf{B} = \mu\varepsilon \frac{\partial \mathbf{E}}{\partial t} + \mu \mathbf{J} \quad (4)$$

where  $\mathbf{E}$  is the electric field,  $\mathbf{B}$  is the magnetic field,  $\rho_f$  is the free charge density,  $\varepsilon$  is the electrical permittivity,  $\mu$  is the magnetic permeability and  $\mathbf{J}$  is the current density. If we assume that the material is an ohmic conductor and that the relationship is isotropic,

$$\mathbf{J} = \sigma \mathbf{E}. \quad (5)$$

Substituting this expression for  $\mathbf{J}$  in Equation (4) we obtain,

$$\nabla \times \mathbf{B} = \mu\varepsilon \frac{\partial \mathbf{E}}{\partial t} + \mu\sigma \mathbf{E}. \quad (6)$$

Taking the curl of Equation (3) we obtain,

$$\nabla \times (\nabla \times \mathbf{E}) = \nabla(\nabla \cdot \mathbf{E}) - \nabla^2 \mathbf{E}. \quad (7)$$

If we assume no free charges, Equation (1) becomes

$$\nabla \cdot \mathbf{E} = 0 \quad (8)$$

and substituting this expression in Equation (7) we obtain,

$$\nabla^2 \mathbf{E} = -\nabla \times (\nabla \times \mathbf{E}). \quad (9)$$

Substituting the expression for  $(\nabla \times \mathbf{E})$  from Equation (3) into Equation (9), and using Equation (6),

$$\nabla^2 \mathbf{E} = \mu \varepsilon \frac{\partial^2 \mathbf{E}}{\partial t^2} + \mu \sigma \frac{\partial \mathbf{E}}{\partial t}. \quad (10)$$

Since snow is nonmagnetic it is appropriate to apply the assumption that the magnetic permeability is that of free space,  $\mu = \mu_0$ . The real effective permittivity,  $\varepsilon_e$  and conductivity,  $\sigma_e$ , which describe the storage and dissipation of energy in an electric field, respectively, are defined using the complex permittivity  $\varepsilon^* = \varepsilon' + \varepsilon''$  and complex conductivity  $\sigma^* = \sigma' + \sigma''$ ,

$$\varepsilon_e = \varepsilon' - \frac{\sigma''}{\omega} \quad (11)$$

$$\sigma_e = \sigma' + \varepsilon'' \omega. \quad (12)$$

The low loss approximation, commonly applied in GPR studies, assumes that  $\sigma'$  is independent of frequency and equal to the DC conductivity,  $\sigma_{DC} \approx 0$  (Olhoeft and Capron, 1994), and that the imaginary permittivity is small compared to the real permittivity. The wave equation is then,

$$\nabla^2 \mathbf{E} = \frac{1}{v^2} \frac{\partial^2 \mathbf{E}}{\partial t^2} \quad (13)$$

in which the velocity can be written in terms of the effective permittivity

$$v = \frac{1}{\sqrt{\mu \varepsilon_e}}. \quad (14)$$

The solution to Equation (13) is of the form

$$\mathbf{E}(\mathbf{r}, t) = \mathbf{E}_0 e^{i(\mathbf{k}\mathbf{r} - \omega t)} \quad (15)$$

where  $k$  is the wavenumber and  $\omega$  is the angular frequency.

The attenuation coefficient  $\alpha$  can be written

$$\alpha = \omega \left[ \frac{\varepsilon_e \mu}{2} \left( \sqrt{1 + \left( \frac{\sigma_e}{\varepsilon_e \omega} \right)^2} - 1 \right) \right]^{\frac{1}{2}}. \quad (16)$$

By using a binomial expansion and applying the low loss approximation, the attenuation coefficient,  $\alpha$ , can be reduced to,

$$\alpha = \frac{\sigma_e}{2} \sqrt{\frac{\mu_o}{\varepsilon_e}}. \quad (17)$$

By substituting Equations (11) and (12) into Equation (17) this becomes

$$\alpha \approx \frac{[\sigma_{DC} + \varepsilon''(\omega)\omega]}{2} \sqrt{\frac{\mu_o}{\varepsilon'(\omega)}}. \quad (18)$$

## 2.2 Spectral Shift Approach for Estimating Liquid Water

Here, the approximation is made that the attenuation is linear with frequency and we introduce the attenuation quality parameter,  $Q^*$ , which is a function of  $\alpha$ ,

$$Q^* = \frac{\omega}{2v\alpha} \quad (19)$$

where  $v = \omega/k$  is the phase velocity as a function of  $k$ , that describes frequency-dependent wave attenuation (Turner and Siggins, 1994). Using  $Q^*$  the attenuation can be written

$$\alpha \approx \alpha_o + \frac{\sqrt{\mu_o \varepsilon'_o}}{2Q^*} (\omega - \omega_o) \quad (20)$$

where  $\omega_o$  is the reference frequency and  $\alpha_o$  is the value of  $\alpha$  at  $\omega_o$ .

A GPR pulse in the time domain,  $R(t)$ , is commonly modeled at the source location by a Ricker wavelet, which is given by

$$R(t) = (1 - 2f_o^2 t^2 \pi^2) e^{-f_o^2 t^2 \pi^2} \quad (21)$$

at time  $t$  where  $f_o$  is the peak frequency.

Using a Taylor expansion to obtain an expression for  $\alpha$  for a bandwidth from some reference frequency  $\omega_o$  for the signal prior to propagation through a medium, we express  $Q^*$  in terms of the complex permittivity

$$\frac{1}{Q^*} = \frac{1}{\varepsilon'_{\omega_o}} \left( \varepsilon''_{\omega_o} + \omega_o \frac{\delta \varepsilon''}{\delta \omega} - \frac{1}{2\varepsilon'_{\omega_o}} \frac{\delta \varepsilon'}{\delta \omega} \right). \quad (22)$$

After propagation through wet snow, liquid water causes frequency-dependent attenuation, which results in a spectrum that has shifted to lower frequencies. Following Bradford (2007), the amplitude spectrum of a Ricker wavelet after propagation is

$$R(t) = \sqrt{2} \frac{\omega^2}{\omega_o} \exp \left( -\frac{\omega^2}{\omega_o^2} - \frac{\alpha(\omega)}{\sqrt{\varepsilon'_{\omega_o} \mu_o}} t \right). \quad (23)$$

For a single point in time, the reflection frequencies that bound the Ricker wavelet through some dispersive material,  $\omega_o$  and  $\omega_t$ , are obtained by setting the time derivative of Equation (22) to zero and including the expression for  $\alpha$  from Equation (20). In this way, the reflection frequencies can be written in terms of  $Q^*$  by

$$\frac{1}{Q^*} = \frac{4}{t} \frac{(\omega_o^2 - \omega_t^2)}{\omega_o^2 \omega_t}. \quad (24)$$

In the case of a radar signal through snow,  $\omega_o$  is the frequency at the snow surface and  $\omega_t$  is the frequency at the snow/ground interface, both of which are calculated from the instantaneous frequency described below. For frequencies below 1GHz, Bradford (2007) shows that the permittivity of water following a Cole-Cole relaxation (Cole and Cole, 1941) can be written in terms of  $Q^*$ , allowing the complex permittivity to be estimated from the frequency content of an attenuated signal,

$$Q_s^* = \frac{\varepsilon'_s}{2\varepsilon''_s}. \quad (25)$$

The center frequency of the Flat Earth radar is approximately 2GHz, so there are portions of the transmitted signal that fall beyond this approximation. For frequencies that are above 1GHz, a scaling factor is calculated that scales those frequencies above 1GHz to what the values would be at 1GHz, which is subsequently applied to  $\epsilon_s''$  as well. Errors introduced by this approximation are detailed below.

### 2.3 Approximations

Several approximations which are made are acknowledged here. First, to apply the constitutive relationship in Equation (5) we assume that the electrical properties of snow are linear and isotropic and that it is an ohmic conductor, which is a common approximation for earth materials. The scales at which these approximations are not appropriate, at the individual sub-cm grain size in snow, are much smaller than the wavelength of the radar pulse and do not affect the bulk properties. Additionally, the form of the radar pulse is modeled with a Ricker wavelet to derive the relationship between the frequencies at the air/snow and snow/ground interfaces and the attenuation quality parameter in Equation (25).

More importantly, the approximation is made that the attenuation is linear with frequency and this is increasingly not the case for frequencies above 1GHz. The effect of this approximation is that the complex permittivity,  $\epsilon_s''$ , is overestimated slightly when it is scaled to the equivalent value at 1GHz by multiplying by  $2\pi \cdot 10^9 / \omega_o$ , which would lead to slight overestimates of the radar velocity (Fig. 3). For a theoretical 2m snowpack with  $\rho = 400 \text{ kg m}^{-3}$  and 0-3% LWC the resulting error in SWE caused by the linearization of  $\epsilon_s''$  is less than 3cm, even at the upper end of the frequency band at 6GHz and 3% LWC. For the field data collected at the tower mounted sites, frequencies above

2GHz were quickly attenuated, and the ground surface reflections were typically below 1GHz.

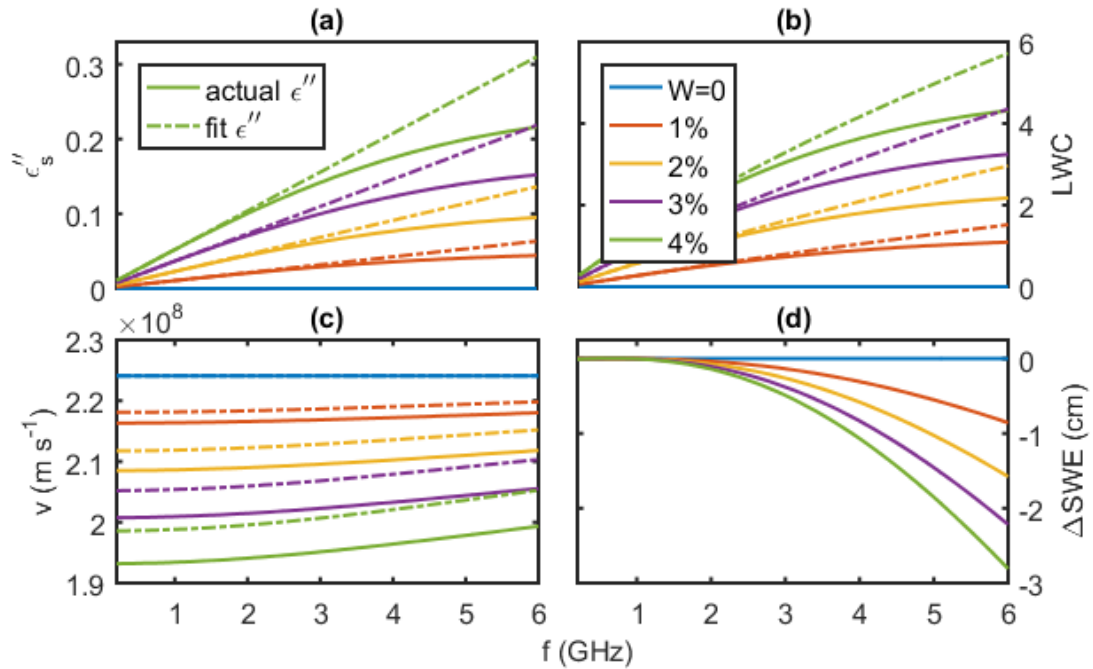


**Figure 3.** Following the complex permittivity of water, the complex permittivity of wet snow exhibits frequency-dependent behavior. All plots are a function of frequency. Subplot (a) shows the frequency dependent behavior of  $\epsilon''_s$  for both actual  $\epsilon''_s$  (solid lines) and the consequence of the assumption of linear fit to  $\epsilon''_s$  (dashed lines) for LWC values from 0-4% (colored lines). The results of the linear fit assumption are shown for LWC in Subplot (b), and the radar velocity in wet snow in Subplot (c). Subplot (d) shows the resulting SWE underestimate that is generated by the linear fit assumption for 0-4% LWC for a theoretical 2m snowpack with a density of  $400\text{kg m}^{-3}$ .

## 2.4 Methods

For tower-mounted, downward-looking radar, the two-way travel time of the radar wave through the snowpack is known after identifying the ground and snow surfaces and calculating the two-way travel time by  $twt = twt_g - twt_s$ , where subscripts  $g$  and  $s$  refer to ground and snow, respectively. Snow depth,  $d_s$ , is known from

$$d_s = 2h_m - \frac{twt_s v_{air}}{2} \quad (26)$$

where  $h_m$  is the mounting height and  $v_{air}$  is the speed of light.

The real component of the permittivity in snow,  $\epsilon'_s$ , is known using  $twt$  and  $d_s$  by

$$\epsilon'_s = \left( \frac{v_{air}}{2d_s} \frac{twt}{twt} \right)^2. \quad (27)$$

$Q^*$  and  $\epsilon''_s$  can subsequently be computed from Equations (24) and (25) and the reflection frequencies, calculated by the instantaneous frequency described below, of the snow and ground surface interfaces. Established empirical relationships then relate dry snow density,  $\rho_d$ , and liquid water content,  $W$ , to the complex electrical permittivity of snow  $\epsilon'_s + i\epsilon''_s$  (Tiuri et al., 1984), where  $\epsilon''_s$  describes the frequency-dependent component,

$$\epsilon'_d = (1 + 1.7\rho_d + 0.7\rho_d^2) \quad (28)$$

$$\epsilon'_s = (0.1W + 0.8W^2)\epsilon'_w + \epsilon'_d \quad (29)$$

$$\epsilon''_s = (0.1W + 0.8W^2)\epsilon''_w \quad (30)$$

where  $\epsilon'_w + i\epsilon''_w$  is the complex permittivity of water and  $W$  is in percent per volume.

The complex permittivity of water following a Cole-Cole relaxation mechanism (Cole and Cole, 1941) is described by Bradford (2007),

$$\epsilon'_w = \frac{(\epsilon_0 + \epsilon_\infty)}{(1 + (2\pi f\tau)^2)} \quad (31)$$

$$\epsilon''_w = \frac{2\pi f\tau(\epsilon_0 + \epsilon_\infty)}{(1 + (2\pi f\tau)^2)} \quad (32)$$

where  $\epsilon_0 = 88$  is the dc permittivity,  $\epsilon_\infty = 4.28$  is the permittivity at infinite frequency and  $\tau = 0.22\text{ps}$  is the relaxation time of water (Fig. 4).

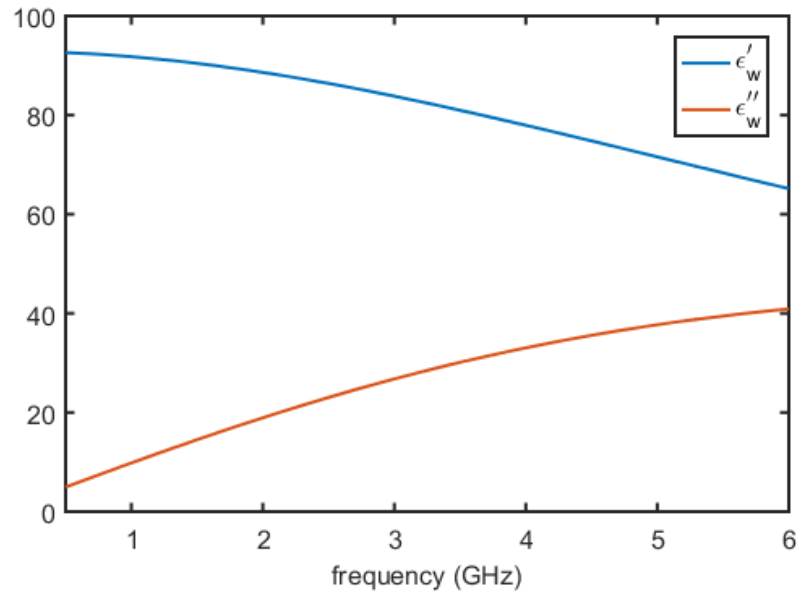


**Figure 4. Values of the complex permittivity of water as a function of frequency.**

The instantaneous frequency (Taner et al., 1979) of the signal is used provide the peak frequencies of the snow and ground surface reflections,  $\omega_o$  and  $\omega_t$ , respectively. For the real, time domain signal,  $R(t)$ , the complex trace is given by,

$$S(t) = R(t) + iy(t) \quad (33)$$

where  $y(t)$  is Hilbert transform of the trace, assuming a symmetric frequency response.

The instantaneous phase,  $\theta(t) = \tan^{-1}(y(t)/R(t))$ , can be computed from the complex signal and the instantaneous frequency is defined as the time derivative of the phase

$$f(t) = \frac{1}{2\pi} \frac{d}{dt} \theta(t). \quad (34)$$

In practice, it was found that a windowed average of two samples of the time derivative of the phase smooths high frequency variation caused by noise and enhances single reflections when applying Equation (34) to field data (Fig. 5).

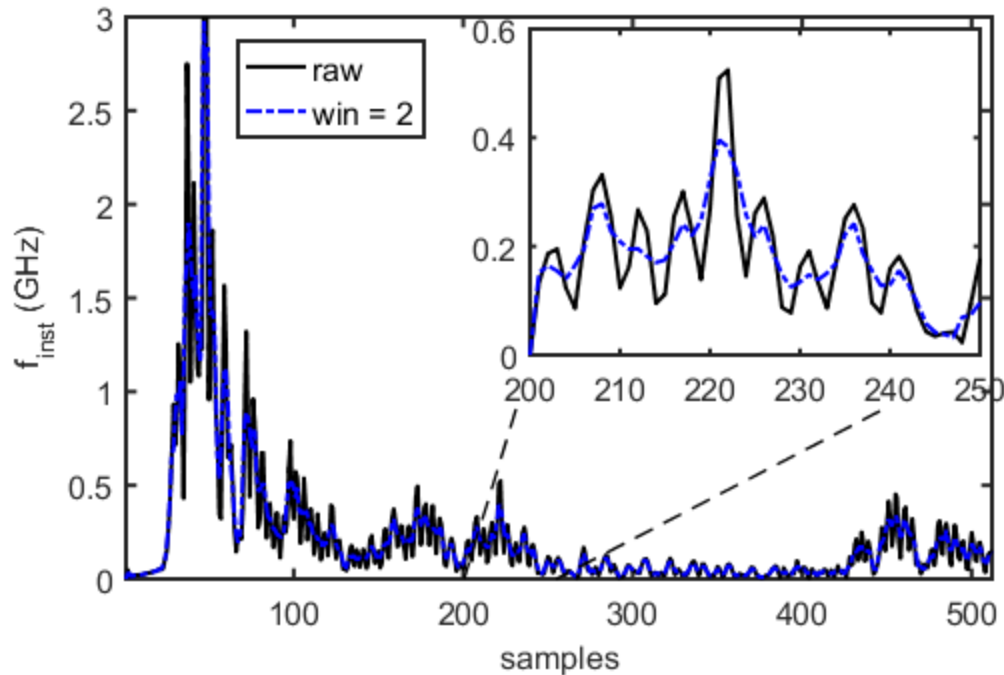


**Figure 5.** Instantaneous frequency (Taner et al., 1979) of a trace from February 1, 2016, at the Banner Summit SNOTEL. Black line shows the instantaneous frequency calculated Equation (34), and the blue dashed line shows the instantaneous frequency using the mean of a two sample window of the instantaneous phase.

### 3 Continuous SWE Measurement with a Low Power Radar System

Although season-long studies of snow properties with radar have been successful in combination with post-processing, continuous and remote deployment of radar for SWE measurements has not become widespread for several reasons. Commercially available radar systems were designed for short field-based surveys, and not with remote or autonomous deployment in mind, which led to difficulty in adapting them to continuous snow measurements. Traditional radar control modules require power on the order of 10W or sometimes even a 60W laptop, which compromises the ability to run on solar power in most cases. Laptop computers and timers have been employed to reduce the continuous power needs, but such systems introduce many more points of failure for a remote system. Traditional interfaces have also required active user input, i.e. a person

pushing a button to trigger a single measurement, and while recorded mouse sequences and laptops have also been applied, it is not a robust approach for continuous remote deployment. Traditional radar systems are also currently significantly more expensive than other methods for remotely measuring SWE, which limits the possibilities for up-scaling and wide application as a SWE sensor.

This study applies established radar techniques to a recently available pulsed radar system from Flat Earth, Inc., which addresses previous limitations for radar remote deployment. The ultra-wideband, 1-6 GHz GPR, built around the Novelda radar chip, was designed to be mounted underneath snow grooming equipment at ski areas to autonomously measure snow depth on ski runs. The robust antenna design, fully configurable on-board microprocessor, low power requirement ( $\sim 4\text{W}$ ) and hands-off measurement collection is well suited for remote sites. We developed a real-time processing algorithm for SWE measurements that was implemented on-board and outputs measured SWE values in near real-time, and in collaboration with Flat Earth, we added an SD card for low-power data logging. The accuracy of the hardware and methods was directly evaluated at a series of snow pits, at which focused radar profiles were performed, coincident with manual measurements. We then deployed the radar SWE sensor with real-time processing at eight fully autonomous sites in Idaho, Colorado and Montana, including seven at remote locations, which continuously measured snow depth, density, liquid water content and SWE. In collaboration with the NRCS in Idaho, radars were installed directly above SNOTEL pillows at the Bogus Basin, Banner Summit and Vienne Mine SNOTEL sites.

### 3.1 Hardware

The Flat Earth impulse system uses a bowtie broadband directional antenna with a center frequency of 2GHz and a gain of 6.5dBi over 1 to 6GHz, and a beamwidth of approximately 70 degrees. The system was designed to operate without user input in winter environments, which allowed for adaptation to tower-mounted sites. The nominal sample time interval is 0.54ps and the receive window is 512 samples. The radar requires 12-30VDC and draws 0.24 amps at 12VDC. It stores the raw signal and settings, applies the onboard processing software, and stores the processed signal on a microSD card. It is capable of transmitting a variety of outputs, including the raw signal, processed signal and calculated SWE estimates, via RS-232.

At tower-mounted locations, the antenna was mounted downward-looking from an arm extended from the tower approximately 100-150cm, and aligned to point normal to the slope. The antenna itself was at least 30cm above the maximum expected snow depth to allow for the direct wave and early time noise. Since the recording window was limited to 27.5ns, the antenna was mounted at maximum height of 300cm above the ground surface. Firmware that stacked two record windows was tested, but since it resulted in some additional noise when the windows were stitched at 27.5ns and the snowpacks of interest were less than 300cm depth, stacked windows were not employed for any of the field studies. Transmit and receive cables were 4m in length, which necessitated mounting the board electronics in a weatherproof enclosure on the tower at approximately the same height as the arm. The measurement interval is programmable, and was set at 15 minutes for these studies. The number of stacks per measurement is also programmable, and a stack of 1000 traces was typically used.

### 3.2 Autonomous Radar Measurement Network

The first Flat Earth radar was installed in March 2014. This system was tower mounted, downward-looking, and solar-powered, and located at Boise State University's Bogus Ridge Snow Research study site near the top of the Dry Creek Experimental Watershed (e.g. Williams et al., 2009), within the Bogus Basin Ski Area, approximately 16 km northeast of Boise, Idaho. Since the spring of 2014, the network was expanded to a total of eight sites in Idaho, Montana, and Colorado (Fig. 6). The radar was installed as a stand-alone unit at each site, with independent solar power, battery bank and mounting arm. This network has logged a combined total of 4.5 years of observations to-date. The site locations and general characteristics are described below (Table 1).



**Figure 6. Locations of eight tower-based radar locations.**

**Table 1.1 Overview of Eight Tower-Based Radar Installations**

	<b>Elevation</b>	<b>Slope</b>	<b>Aspect</b>	<b>Installation</b>
Bogus Ridge Snow Research Site, near Dry Creek Experimental Watershed (DCEW)	2114	20	SE	Mar 2014
Bogus Basin SNOTEL	1932	0	-	Dec 2014
Banner Summit SNOTEL	2145	0	-	Nov 2015
Vienna Mine SNOTEL	2731	0	-	Aug 2015
Garden Mountain	2040	0	-	Dec 2015
Fraser Experimental Forest	2773	0	-	Nov 2015
Red Mountain Pass	2584	0	-	May 2015
Flat Earth, Inc. (test site)	1363	0	-	Jan 2016

(1) The Bogus Ridge study site is located within the bounds of the Bogus Basin ski area at an elevation of 2100m, near the top of the Dry Creek Experimental Watershed. It is approximately 20m below a ridge top, leeward of the prevailing wind direction. The mounting tower is a 10cm steel pole sunk in concrete, and the immediate vicinity is extensively studied with a wide range of geophysical equipment, and includes nearby measurements of temperature, wind, radiation and snowmelt at sloped and flat-ground lysimeters. The radar itself is on a lightly treed, southeast aspect, and sits on a 20 degree slope. The site has seen snow packs up to 150cm in depth from the period March 2013 to April 2016. Owing to the relatively low elevation and southeast aspect, this site often has measurable liquid water content, as well as freeze/thaw layers within the snow pack and ice lenses at various points during the winter season. There are a few trees spread out across the site and the radar footprint is in a small clearing with shrubs. The shrubs were cleared so that the radar footprint is a planar surface on mostly bare ground. A section of

the slope is saved for snow pits measurements, which are approximately 10m upslope of the radar footprint on a similar slope angle. The site is powered by a nearby solar installation with two 100W solar panels and an approximately 300amp-h battery bank that supplies power to the radar as well as other instruments.

(2) The Bogus Basin SNOTEL, also in bounds at the Bogus Basin ski area, is at 1860m elevation approximately 0.5km northwest of the Ridge site, with the radar installed in December, 2014. As with all co-located SNOTEL network sites, the radar footprint matches the SNOTEL pillow to the greatest extent that is practically possible, and the majority of each footprint measures the same snow. The radar antenna is mounted on an arm that extends 80cm from the tower, which also supports the ultrasonic depth sensor. It is the least wind-protected of the three co-located SNOTEL sites and has snow pack depths up to 180cm since measurements began. This site is generally shaded by trees and the slope immediately south during the winter months and typically receives more snow and experiences fewer melt-freeze days than the nearby Bogus Ridge site. The radar is powered by a 100W solar panel and an initial ~60amp-h battery bank that was expanded to ~130amp-h in December, 2015, after a cloudy period that resulted in several power failures.

(3) The Vienna Mine SNOTEL is located in the Smiley Creek drainage of the Sawtooth Mountains of central Idaho, at an elevation of 2730m. The Vienna Mine SNOTEL site typically sees one of the deeper snow packs measured by the Idaho SNOTEL network, and recorded a maximum snow depth of 280cm during the period of coincident radar measurement beginning in August, 2015. The site is in a northeast facing cirque approximately 600m below the ridge and is relatively sheltered from high winds.

Although it does receive some direct sun during the winter, it is typically a dry snow pack for most of the accumulation season, owing to the high elevation. The radar is powered by a 100W solar panel and ~150amp-h battery bank. Sections of private land ownership, distance from the road, and avalanche terrain make this site difficult to visit in winter.

(4) The Banner Summit SNOTEL is located in a small clearing in a forested, sheltered area, approximately 0.5km west of Banner Summit, Idaho, at 2145m (Fig. 7). The site also sees some direct sun, even during winter months, and generally maintains subfreezing temperatures, although some liquid water in the pack is not uncommon mid-winter. It received a maximum snow depth of 230cm for the 2016 winter during coincident radar measurements, which began in November, 2015. The radar is powered by a 100W solar panel and the original ~110amp-h battery bank was expanded to ~150amp-h after a period of snow covering the solar panel resulted in power loss from November to early January, 2016.



**Figure 7.** Banner Summit SNOTEL site, approximately 0.5km west of Banner Summit, Idaho. The foreground tower holds two arm mounts: the upper arm holds the NRCS ultrasonic depth sensor, and the lower arm supports the radar antenna, with orange frame and white enclosure facing downward that covers the bowtie antenna. The radar ground footprint is approximately  $12\text{m}^2$ , most of which overlaps the SNOTEL snow pillow directly underneath, although the bottom of the tower is also in the field of view. The desire to have the radar and SNOTEL pillow footprints overlapping to the greatest possible extent resulted in a non-ideal antenna mounting configuration, in which the base of the tower was within radar footprint. This caused difficulty in selecting the ground surface reflection.

(5) The Garden Mountain site is a weather station operated by Idaho Power Corporation in the west central mountains, approximately 10km northeast of Banks, Idaho. The weather station is in an open clearing at 2040m elevation and receives direct sun all year. Several high resolution precipitation gauges are installed at this site. The radar was installed December, 2015, and measured a maximum of 170cm snow depth

through April, 2016. At this site, radar-derived SWE measurements are compared with the accumulated precipitation from the gauges.

(6) The Fraser Experimental Forest is a well-instrumented United States Forest Service research site in Colorado. This radar was installed at the ground level, and is upward looking. Meteorological, snowpack, and soil observations are recorded hourly. This site also includes a side-looking 6-18GHz FMCW radar system and has been the location of several large NASA snow remote sensing field campaigns.

(7) Senator Beck Basin, operated by the Center for Snow and Avalanche Studies, is a small research watershed at the headwaters of the Uncompahgre Basin, which is one of the major tributaries of the Colorado River. The site is one of only a few high alpine sites with full energy-balance observations, with meteorological stations both above and below treeline. We installed a Flat Earth radar system at the lower station at an elevation of 11,100 ft, in a wind protected clearing, in Spring, 2015.

(8) A test unit was also installed at the Flat Earth headquarters in Bozeman, MT. The radar was installed and has been running continuously since January, 2016, though its intended use is testing firmware updates and power requirements, rather than reporting SWE values.

### 3.3 Signal Processing

#### 3.3.1 Tower Based Measurements

The signal processing for tower based measurements consists of four components: (1) correction of the sample interval, which is variable and depends on the radar chip temperature; (2) resampling of the trace using the actual sample interval; (3) normalization of the amplitudes; and, (4) time zero correction.

(1) A correction to the sample interval was necessary due to temperature effects on the chip hardware, which resulted in sample interval variations that affected the apparent frequency and travel time. Chip temperature is recorded along with the raw data, and was used to make the correction. Periods of field data were extracted during times when the snow surface reflection was obvious and SWE was known to be constant, confirmed with ultrasonic depth measurements and precipitation observations from the SNOTEL. Air temperatures were sub-freezing both prior to and during these periods of consistent snow depth, and the radar showed no significant variations in reflection frequencies between the snow and ground surfaces. Despite the consistent snow depth, both the snow surface and ground surface vary significantly in apparent time, correlated with each afternoon warming period, and also with respect to each other (Fig. 8). A section of raw data shows the variability in time of the snow and ground surface reflections prior to sample interval correction (Fig. 8(a)). The variable number of samples between the snow and ground surfaces and the temperature recorded on the radar chip is shown in Fig. 8(c). Assuming that the distance between the snow and ground surfaces is not, in fact, changing in time and the radar velocity is constant ( $LWC = 0$ ), the number of samples between them should be constant. During this time period, however, a constant sample interval leads to variable two-way travel time between the snow and ground interfaces in a snowpack that is not changing. An adjusted sample interval is calculated, as a function of temperature and fit to a second order polynomial, for the interval required to have a constant two-way travel time between the snow and ground interfaces. The corrected sample interval,  $dt_c$ , is

$$dt_c = T^2 2.39 \times 10^{16} + T 8.21 \times 10^{-14} + 5.24 \times 10^{-11}. \quad (35)$$

The radar signal is resampled to the corrected sample interval, and then the surfaces no longer vary in time in the radargram. The corrected sample interval, as a function of chip temperature, was subsequently applied to all data in Step (2).

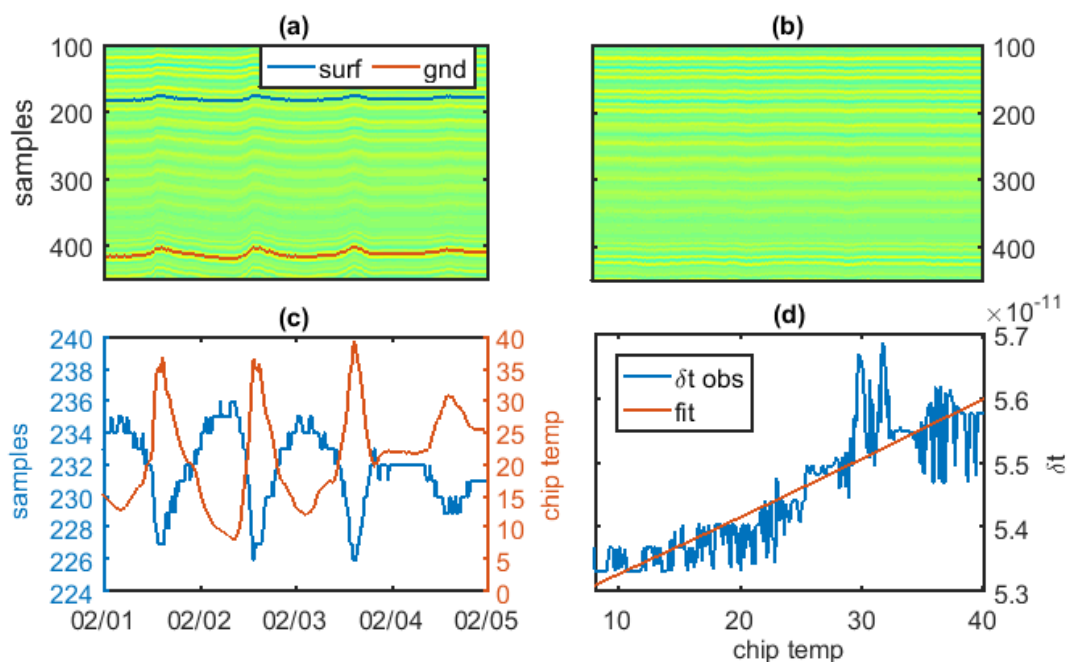


**Figure 8** A temperature correction to the effective sample rate was created from field data and applied to all other data sets. Subplot (a) shows field data from four days at the Banner Summit SNOTEL in which the snow surface (blue) and ground surface (orange) are visible. It was a calm period at the SNOTEL site and the ultrasonic depth sensor showed no change in snow depth, ambient temperature was sub-freezing and the radar showed no significant LWC. Despite this, both the snow surface and ground surface vary significantly in time each afternoon, and also with respect to each other. Subplot (b) shows the varying number of samples between the snow and ground surfaces (blue line) and the temperature recorded on the radar chip (orange line). Assuming that the distance between the snow and ground surfaces is not, in fact, changing in time and the radar velocity is also not changing ( $LWC=0$ ), the sample interval required to meet this assumption is calculated. This estimated sample interval is modeled as a quadratic function of temperature. The radar signal is then resampled to the corrected sample interval, as shown in (b), and then the surfaces are seen to no longer vary in time in the radargram.

(2) Once the corrected sample interval was obtained, it was applied to each trace.

Since each trace contains 512 samples, the actual receive window was longer in cases where the chip hardware was sampling with a decreased interval. Resampling the trace to

the corrected interval was helpful, rather than simply applying the corrected sample interval for each trace, for the automatic algorithm that picked the snow and ground surface reflections. For traces in which the actual sample interval was slower than the nominal sample interval, the trace was truncated at the end of the resampled window. This shortened trace was then interpolated to the corrected number of samples.

(3) Ambient chip temperature also affected the mean signal amplitude (Fig. 9). Since trace amplitudes are not used in an absolute sense, they were normalized so that the direct wave had a maximum amplitude of one. This was also helpful when applying the automatic processing algorithm, which picked the snow and ground surface reflections.

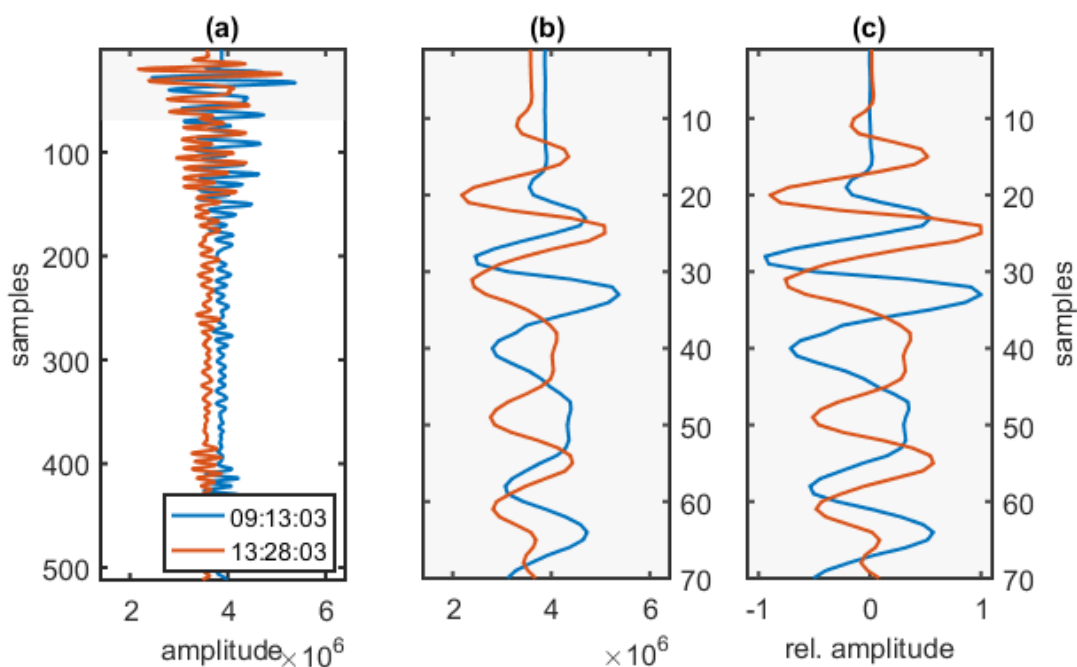


**Figure 9.** Two traces taken several hours apart on January 28, 2015 at the Bogus SNOTEL. Subplot (a) shows the difference in mean trace amplitude between the two traces, and Subplot (b) details the differences in the direct wave for the same two traces. Subplot (c) shows the traces with the peak in the direct wave set to one.

(4) Lastly, the peak in the direct wave was set to time zero (Fig. 10).

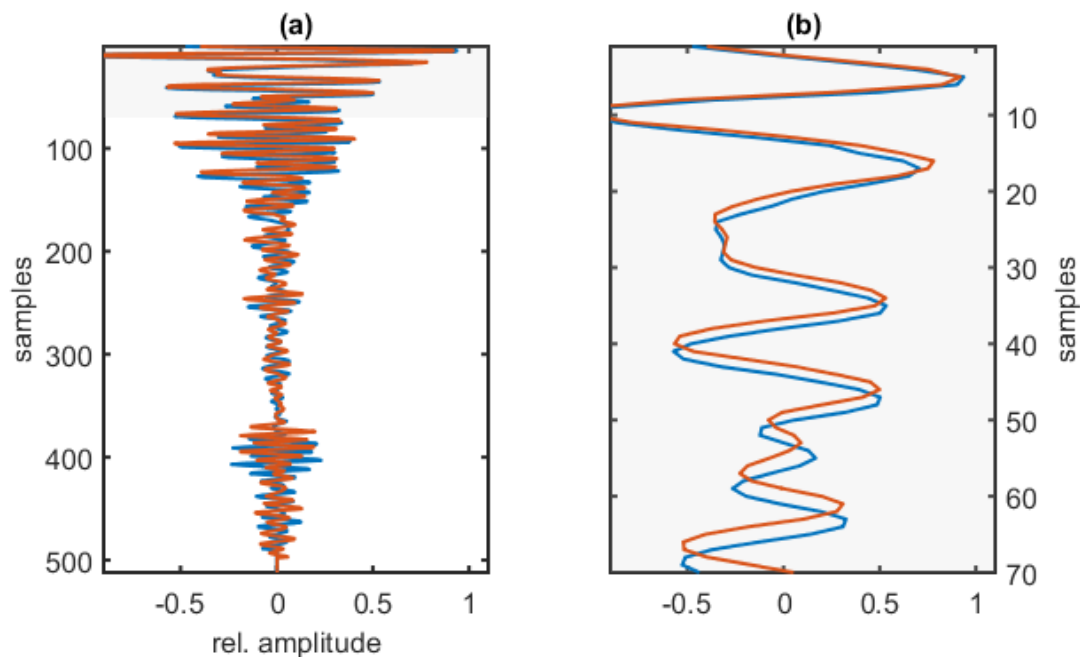


**Figure 10.** The same two traces in Fig. 9 are shown with the trace set to time zero at the peak in the direct wave, with the full trace in Subplot (a) and detail of the first 70 samples in Subplot (b).

Although some dampened daily-scale variations in the ground surface remained after the temperature correction, resampling and time-zero correction (e.g. 1-3 sample variations in the ground surface reflection during cold periods, with no daily-scale change in ground surface reflection frequency or change in snow depth), these steps greatly improved the coherence of reflections in the raw radar signal (Fig. 11). These steps are a critical component of the automatic algorithm for surface picking and SWE calculation described below.

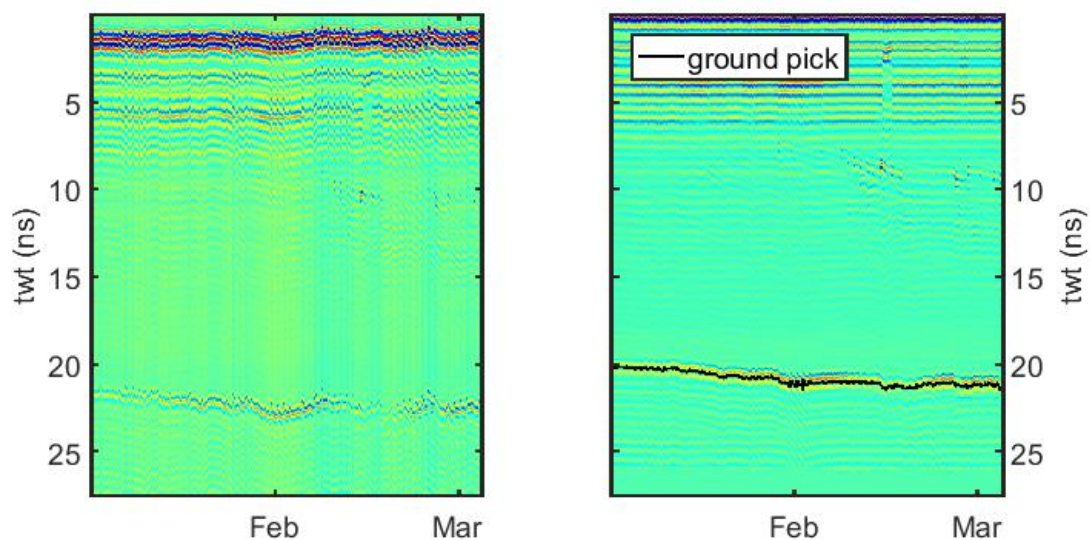


**Figure 11. Raw and processed signals for the Garden Mountain site for the period January 3 – March 5, 2016, showing a more coherent ground reflection after trace processing. Significant daily-scale variations in two-way travel time to the ground reflection, which appears between 20 and 25ns, are corrected so that changes greater than 1-3 samples in the ground reflection correspond to changes in SWE.**

### 3.3.2 Snow Pit Measurements

For profiles over the snow pits, fewer processing steps were performed on the traces. Although there was not significant variability in trace amplitude over these brief collections, trace amplitudes were still normalized. Temperature-based sample interval correction, resampling and time zero correction were not applied because these did not cause significant changes over the course of the period of collection.

For the focused profiles taken immediately prior to manual snow pit excavation, the radar antenna was mounted to a 2m length of PVC tubing so that the antenna footprint was extended from the observer and possible interference. Once traces were being collected, the antenna was slowly lifted from the snow surface to ~100cm above the snow surface, and then moved laterally across the snow pit area, ~100cm, at a height of 50 – 100cm. The up/down movements of the antenna distinguished the snow and ground

interfaces, as they moved in time and constant system noise did not. Snow and ground surfaces were picked by hand as the largest negative peaks (Fig. 12). Since the antenna was held by hand and the surfaces were still varying a small amount in time, the two-way travel time and instantaneous frequency calculations were taken as the median over several traces, typically 10 – 20.

Calculation of radar velocity in snow,  $v = dt$ , was made with independent measurements of depth,  $d$ , measured at the snow pit, and travel time,  $t$ , from the snow and ground surface picks in the radar profile. Once depth and velocity were calculated, density was calculated from Equations (28) – (30), and subsequently SWE.

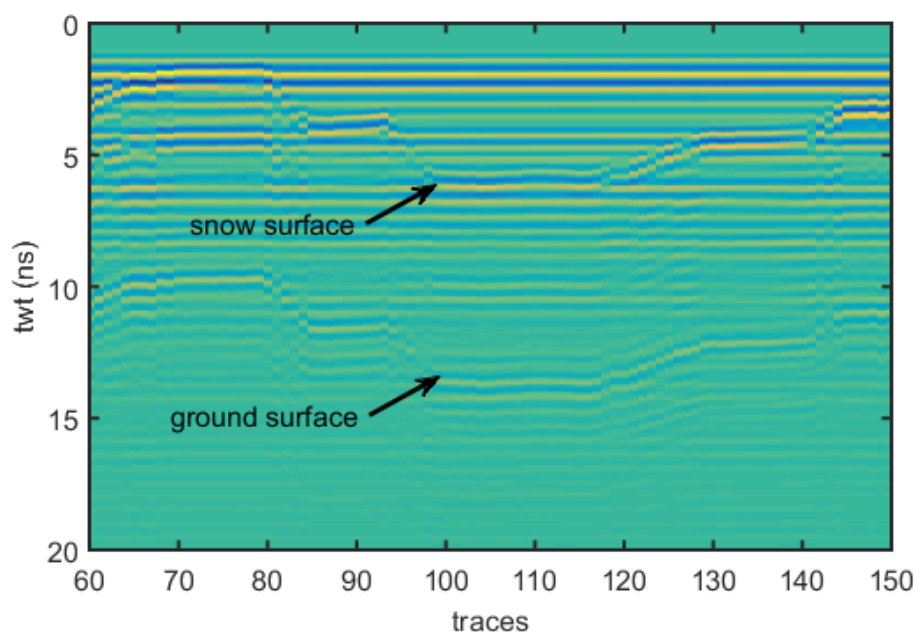


**Figure 12.** Focused radar profile prior to manual snow pit excavation at the same location. In this representative profile the radar antenna was moved vertically by hand from approximately 0-90cm above the snow surface. For a single trace the snow and ground surface reflections are difficult to distinguish, but with antenna movement they separate from constant system noise. Snow and ground reflections are picked by hand over 10-20 traces, from which the two-way travel time is calculated.

### 3.4 Real-Time Algorithm

Once a raw signal was collected every 15 minutes at the tower-mounted sites, a processed trace was automatically generated using the steps described in Section 3.3.1. The processed trace was then input to an algorithm, described below, and a SWE calculation was made in two ways.

#### 3.4.1 Dry Snow

The first method, applied in all circumstances and appropriate for dry snow conditions, uses the difference in travel time between when the ground would appear in snow-free conditions and when it appears with snow-on. The two-way travel time at which the ground surface reflection appears during snow-off conditions,  $twt_a$ , is

$$twt_a = \frac{2d}{v_{air}} \quad (36)$$

where  $v_{air} = 3 \times 10^8 \text{ m/s}$  and  $d$  is the distance above the ground. The radar velocity in snow,  $v_s$ , can be written in terms of  $v_{air}$  and the radar velocity in ice,  $v_i$ , using  $\emptyset = \left(1 - \frac{\rho_s}{\rho_i}\right)$ ,

$$\frac{1}{v_s} = (1 - \emptyset) \frac{1}{v_i} + \emptyset \frac{1}{v_{air}} \quad (37)$$

where  $v_i = 1.68 \times 10^8 \text{ m/s}$ . Following this, the two-way travel time to the ground,  $twt_s$ , with some depth of snow,  $d$ , can be written,

$$twt_s = 2d \left( \frac{\rho_s}{\rho_i v_i} + \frac{1}{v_{air}} - \frac{\rho_s}{\rho_i v_{air}} \right). \quad (38)$$

The difference in snow-off and snow-on travel times,  $twt_d = twt_s - twt_a$ , is

$$twt_d = d\rho_s \left( \frac{2}{\rho_i v_i} - \frac{2}{\rho_i v_{air}} \right). \quad (39)$$

By applying the known constants  $v_i$  and  $\rho_i = 0.934 \text{ g/m}^3$  we get,

$$\frac{twt_d v_i}{\rho_i} = d\rho_s. \quad (40)$$

Since SWE is obtained by converting the depth of ice in a snowpack to a depth water by multiplying by  $\rho_i$ , this shows that  $twt_d$  is proportional to SWE.

The ground surface reflection pick,  $r_g$  in samples and  $r_g dt$  in time, is the highest amplitude reflection of the envelope of the signal  $S(t)$ , Equation (33), between  $twt_d$  and the end of the receiving window. In the dry snow case, SWE can be written as a function of only the ground surface pick and the mounting height,

$$SWE = \frac{v_i \left( dt * r_g - \frac{2hm}{v_{air}} \right)}{2}. \quad (41)$$

This method has the benefit of not requiring a snow surface pick, and is not dependent on snow depth or density. It does assume no liquid water, however, and if this assumption is wrong it gives an overestimate of SWE by virtue of the decreased velocity caused by water.

### 3.4.2 Wet Snow

In all cases calculations are also made which include calculation of the spectral shift and LWC. The time delay,  $twt_d$ , is useful in two ways. A snow depth estimate,  $d_e$  can be made by

$$d_e = v_i twt_d \rho_i \rho_e^{-1} \quad (42)$$

where  $\rho_e$  is a snow density estimate. A low and high density estimate, such as  $\rho_e = 200 - 420 \text{ kgm}^{-3}$ , are used to make low and high snow depth estimates, which are in turn used to make reasonable window bounds for where the snow surface reflection could be expected to occur in time. The snow surface pick,  $r_s$ , is the highest amplitude reflection of the envelope within the expected window in the same manner as  $r_g$ . With

both snow and ground surfaces picked, the two-way travel time in snow,  $twt_s$ , is calculated from

$$twt_s = (r_g - r_s)dt. \quad (43)$$

Snow depth,  $d_s$ , is obtained from

$$d_s = h_m - (v_a r_s dt)/2. \quad (44)$$

Once  $d_s$  is known the radar velocity  $v_s$  is found by

$$v_s = \frac{2d_s}{twt} \quad (45)$$

and the real component of the permittivity is

$$\varepsilon' = \left(\frac{v_a}{v_s}\right)^2. \quad (46)$$

Following Bradford (2009), the signal frequencies of the snow and ground surface reflections,  $\omega_o$  and  $\omega_t$  respectively, are the maxima of the instantaneous frequency within a wavelength centered at  $r_s$  and  $r_g$ , respectively.

Once  $d_s$ ,  $v_s$ ,  $\omega_o$ ,  $\omega_t$  and  $\varepsilon'$  are known,  $Q_s^*$  is calculated from Equation (24) and  $\varepsilon''$  is calculated from Equation (25). Finally,  $\rho_d$  and  $W$  are calculated from Equations (28) – (30) and SWE is

$$SWE = \rho_s d_s. \quad (47)$$

Once the calculations are complete,  $v_s$  and  $\rho_s$  are input to an error function: since reasonable upper and lower bounds on  $v_s$  and  $\rho_s$  are known for seasonal snowpacks, these can be used to check the reasonableness of the snow surface pick. Upper and lower bounds for both  $v_s$  and  $\rho_s$  are updatable parameters for the algorithm, but were generally set as

$$v_{low} = 0.18 \text{ m ns}^{-1}$$

$$v_{hi} = 0.245 \text{ m ns}^{-1}$$

$$\rho_{low} = 200 \text{ kg m}^{-3}$$

$$\rho_{high} = 420 \text{ kg m}^{-3}.$$

If the calculated velocity or snow density was outside of these set limits, the error function outputs an adjusted, new window for the surface picking. For example, if  $r_s = n$  and  $v_s < v_{low}$ , the new surface picking window was set to end at  $n - 1$  samples.

A triggered error and reset surface picking window was counted as an iteration, and the number of iterations to run while calculating parameters and SWE was limited to 20, after which all values for that traces were flagged as error. For a relatively small window size of 15 samples, 20 iterations over a new window size gives a range of up to 300 samples. Since the ground surface reflection arrives at approximately 360 samples in snow-free conditions, this is more iterations than is necessary. In practice, given the number of samples within the full trace and initial surface pick window based on  $twt_a$ , the algorithm only hit the full iteration limit and reported error values in the rare cases in which the raw trace was erroneous. Outside of a single instance of antenna failure, described below, errors in the raw traces were not persistent.

### 3.4.3 Ground Picking

As described above, the ground surface reflection pick  $r_g$  is typically taken to be the highest amplitude reflection of the absolute envelope of the trace (Eq. 33) between  $twt_a$  and the end of the receiving window; however, the complete process is described here.

In practice, the initial pick,  $r_i$ , of the highest amplitude reflection of the envelope of the trace faced two potential difficulties. The first is that while  $r_i$  most often selected

what was interpreted to be the actual ground surface reflection, small variations in a few traces, such as could be described by liquid water briefly pooling at a deep pack interface or rare erroneous traces, resulted in the highest amplitude of the envelope not always corresponding to the ground surface. Secondly, the temperature effect on the sample interval, while mostly corrected by the processing steps described in Section 3.3.1, still resulted in the ground surface reflection varying in time by a few samples on a daily scale.

To overcome these challenges, the algorithm stores two ground surface picks for each measurement. The initial pick of the highest amplitude reflection of the envelope of the trace within the specified ground window,  $r_i$ , was stored first. After the radar was in operation for greater than a defined number of measurements, typically 30,  $r_i$  was compared to the median of the previous picks within that window. If  $r_i$  was within  $\pm 3$  samples of the median of the previous picks, the final ground surface pick,  $r_g$  was set equal to  $r_i$ . If  $r_i$  was outside of expected bounds,  $r_g$  was selected as the median of the 30 previous measurements of  $r_i$ . This method not only smoothed the approximately  $\pm 3$  sample daily-scale variation remaining from the temperature effects on the sample interval, it also avoided single-trace spikes in highest amplitude of envelope which occasionally occurred (Fig. 13). This method introduces a sub-30 measurement lag in changes in the ground reflection, but the benefits of smoothing single-measurement variation justify this.

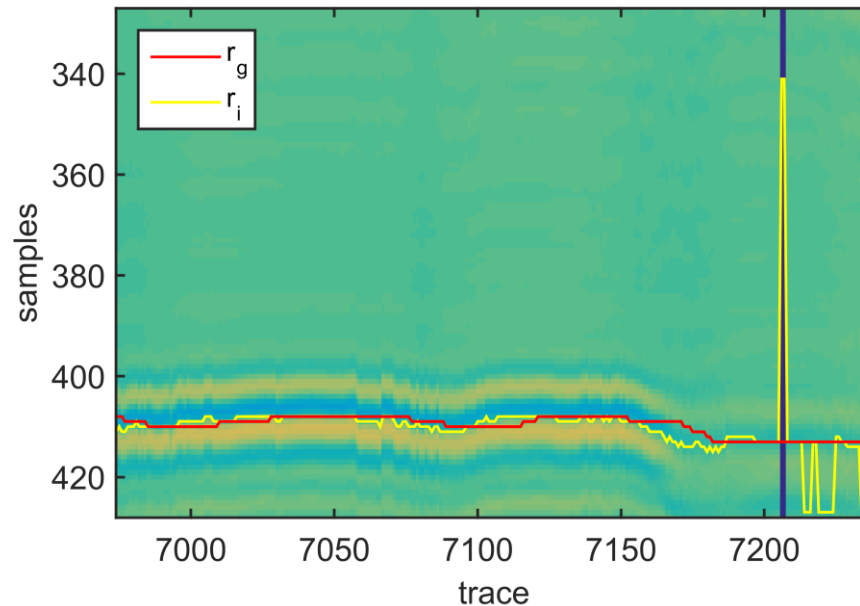


**Figure 13.** Background color is the absolute envelope showing the ground surface reflection at 400-420 samples at a section of data from the Garden Mountain site, March, 2016. The initial ground picks,  $r_i$ , are shown in yellow, and can be seen to have a  $\pm 3$  sample variation that is a remnant of the temperature correction to the sample interval. When the signal has undergone more attenuation around trace 7170 and the ground surface reflection becomes less clear  $r_i$  also spikes significantly to other peaks. The final ground picks,  $r_g$ , shown in red and the median of the previous 30 values of  $r_i$ , smooth both the single-trace and significant spike variability. The result of the 30 trace window median can also be seen in the slight lag in  $r_g$  responding to the dip in ground surface reflection around trace 7090.

Objective or independent assessment of the ground pick is not available in this algorithm, which exhibited different results based on the quality of the physical tower-mounted antenna setup with respect to the radar footprint. For the Garden Mountain site, in which the antenna was mounted on a 150cm arm and the tower itself was much less in the antenna footprint, and the only significant reflection was from the ground, the ground reflection and initial pick were within  $\pm 3$  samples of what the researcher would have interpreted the ground reflection to be for over 99% of the measurements. For the SNOTEL sites, there were multiple possible reflections within a 1ns of the snow/ground interface, including: the snow/ground interface itself; the top of the SNOTEL antifreeze

pillow (which could potentially be a distinct surface due to additional heat flux through the pillow and base of the snow pack melt); the base of the antifreeze pillow; and the base of the tower itself. The result was that there were frequently several reflections near in time to when the ground surface reflection was recorded, all of which varied in amplitude. The algorithm supports an updatable ground surface window, in which the user can force the algorithm to use a pre-defined window of samples in which to look for the maximum amplitude reflection of the envelope, as well as the number of measurements to apply the forced window. For example, with some prior knowledge of the snowpack and SWE at a given site, such as a user would obtain on a site visit, the user could force the algorithm to look for the ground reflection within samples 400:425 of the full 512 sample trace, rather than from sample 375 (where it may have appeared in snow-off conditions) through the full 512 samples, and to apply that for 1000 measurements. This updatable window proved very useful for the non-ideal mounting at SNOTEL sites and, in most cases, could successfully guide the algorithm through a winter season with a realistic number of window updates corresponding to site visits. At the Garden Mountain site, in which the antenna was mounted on a longer arm extending from the tower and  $\sim 2\text{m}^2$  of chicken wire was placed on the ground surface to enhance the snow/ground interface, the ground surface reflection was clear, and the updatable window was not necessary.

## **4 Results**

### 4.1 Comparison to Manual Snow Pits

The most direct, repeatable method of evaluation of radar-derived SWE was comparison to manual snow pit measurements. The accuracy of the radar in measuring

snow depth, SWE and, when present, LWC, was directly evaluated over a series of 15 snow pits. For this evaluation, the radar antenna was typically mounted to a 2m section of PVC tubing to extend the footprint away from the researcher and over undisturbed snow where the manual snowpit measurements were later performed. The radar itself was powered and triggered by a tablet computer and the footprint area was subsequently excavated. Manual measurements of snow depth, density and temperature were collected. Snow density was typically measured with a 250 or 1000cc cutter at depth intervals of 10cm, with two side-by-side measurements for each depth interval. When snowpack temperatures were warm enough for liquid water to be present, liquid water content was also measured at 10cm intervals with the Finnish Snow Fork (Tiuri et al., 1984). The series of 15 snow pits resulted in ranges of observed snow pit depth from 55-100cm, bulk density from 270-450kg m<sup>-3</sup>, bulk 0-4% LWC and a resulting range in SWE from 21-36cm.

The range in observed density in the pits is an important consideration for snow measurements, since if ignored, the combination of ranges in depth and density in these pits leads to up to 30% difference in SWE (Lundberg and Thunehed, 2000). Given that snow density changes both spatially and temporally, reliance on depth information alone introduces error. Using snow pit measurements of depth, radar calculations of density are compared with pit density over a series of 15 pits (Fig. 14). Uncertainty in measured snow density is typically on the order of  $\pm 9\%$  (Proksch et al., 2016), and this constant density uncertainty is shown with errorbars in Figure 14. For 12 of the 15 pits, the radar density was within the error that could be expected from manual pit density measurement, demonstrating that the radar is accurately measuring snow density given

independent depth information. Direct observation of snow density is time consuming and destructive, therefore this application of radar for estimating density time series is a valuable step forward in snow monitoring.

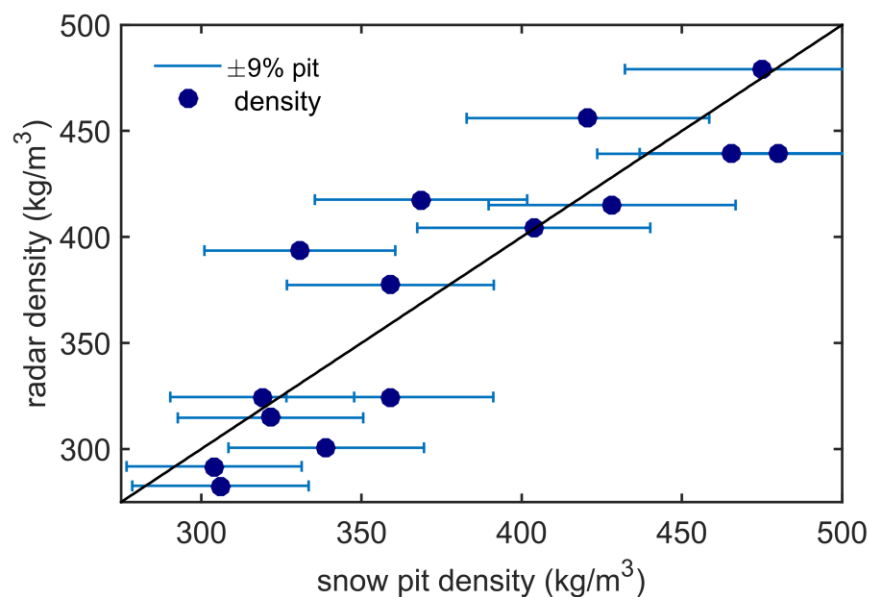


**Figure 14.** Using snow pit measurements of depth, radar calculations of density are compared with pit density over a series of 15 pits. Error bars on the manual snow pit density are  $\pm 9\%$ . For 12 of the 15 pits the radar density was within  $\pm 9\%$  of the manual density.

Since SWE is a function of snow density, errors in the radar measurements of SWE followed those of density (Fig. 15). Radar-derived SWE was within the uncertainty of the manual measurements,  $\pm 9\%$  density multiplied by depth, for 12 of the 15 pits. There was a slight positive bias in radar-derived SWE, as across all 15 snow pits the percent error in SWE was  $2 \pm 8\%$ , and the absolute percent error was 7%.

It is instructive to consider the consequences of choosing an arbitrary density measurement to the range of observed depths. In this case, if a single arbitrary density of  $320 \text{ kg m}^{-3}$  is applied, the number of radar measurements that fall within the uncertainty of the manually derived SWE drop from 12 to 5.

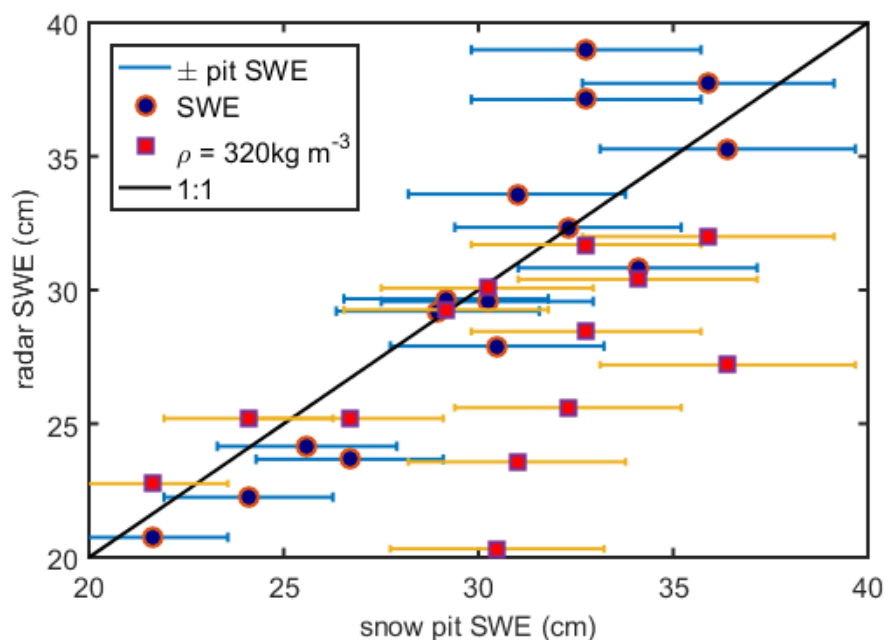


**Figure 15.** Using snow pit measurements of depth and radar measurements of density, radar calculations of SWE are compared with pit SWE for the same series of 15 pits as in Figure 14. Error bars for the manual SWE are  $\pm 9\%$  multiplied by the pit depth. For 12 of the 15 pits the radar SWE was within the uncertainty of the manual measurements. Red squares shown the consequences of an arbitrarily chosen density, in this case  $320\text{kg m}^{-3}$ , applied to the independent depth measurements. For this arbitrary density the number of radar estimates of SWE that fall within the manual SWE uncertainty drop from 12 to 5.

#### 4.1.1 Liquid Water Content

Radar-derived LWC was compared to Snow Fork values using the tower-mounted radar at the Bogus Ridge site from the 2014 season. Semi-weekly snow pits were excavated from a location approximately 10m upslope of the tower-mounted radar. The snow pit locations were on the same slope and aspect as the tower based radar, but received slightly less mid and late-day shading from nearby trees as compared to the tower site. Snow Fork measurements were collected as the last measurement for each of the snow pits, following temperature, density and grain size measurements, which may have led to artificially higher LWC values measured by the Snow Fork, as the snowpack had up to several hours to drain to the edge of the pit face. LWC measurements were

collected at 10cm depth intervals, and a bulk average was compared with radar-derived LWC (Fig. 16). The radar LWC is reported as the mean over 50 measurements from each snow pit collection day, spanning approximately 10am – 10pm.

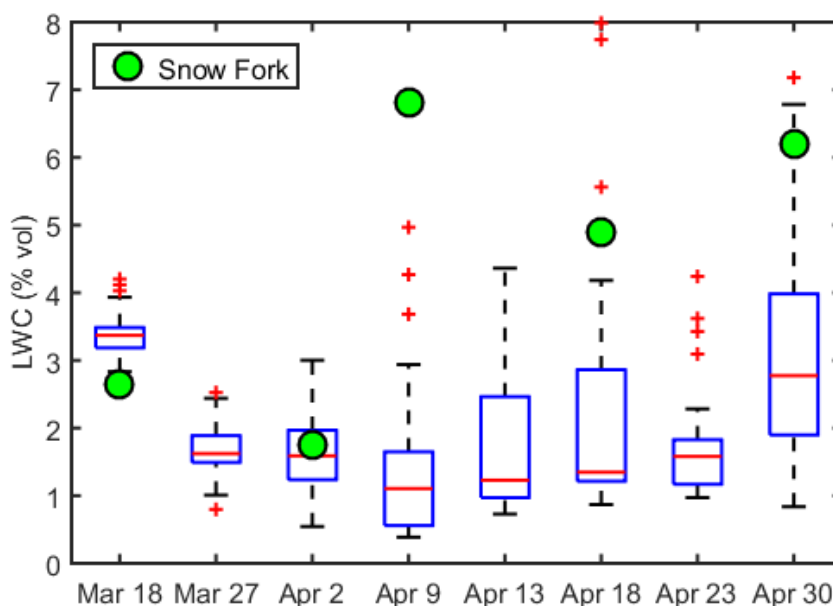


**Figure 16.** Radar-derived LWC values for 12 hour daytime periods at the 2014 Bogus Ridge Site are shown as boxplots for days when manual snow pit measurements were also collected. Snow Fork values, as the mean of all values taken at 10cm intervals, are shown as green circles. Although the correlation between median radar-derived LWC and mean Snow Fork values is low, high Snow Fork values can be explained from those measurements being collected last in the snow pit, giving the pack time to drain to the pit face. Radar-derived LWC are physically reasonable and the presence of water is corroborated by Snow Fork measurements.

Although the correlation between radar-derived and Snow Fork LWC is low, the ability of the radar to detect LWC amounts within a physically reasonable range is important, and there is a linear improvement in SWE calculation in the presence of liquid water. For example, for a 20ns two-way travel time in a snow pack with mean density of  $400\text{kg m}^{-3}$ , a range of 0-4% LWC corresponds to a 25cm range in snow depth and a nearly 10cm range in SWE. Thus, for every 1% increase in LWC that is unaccounted for

there is a 2cm overestimate of SWE in this theoretical snow pack (Fig. 17). The mistake of collecting Snow Fork measurements at the end of each snow pit, while the water had time to drain downhill and collect at the pit edge, likely led to an overestimation of LWC which made direct, quantitative comparisons difficult. Other work has indicated the Snow Fork may overestimate LWC (Techel and Pielmeier, 2011).

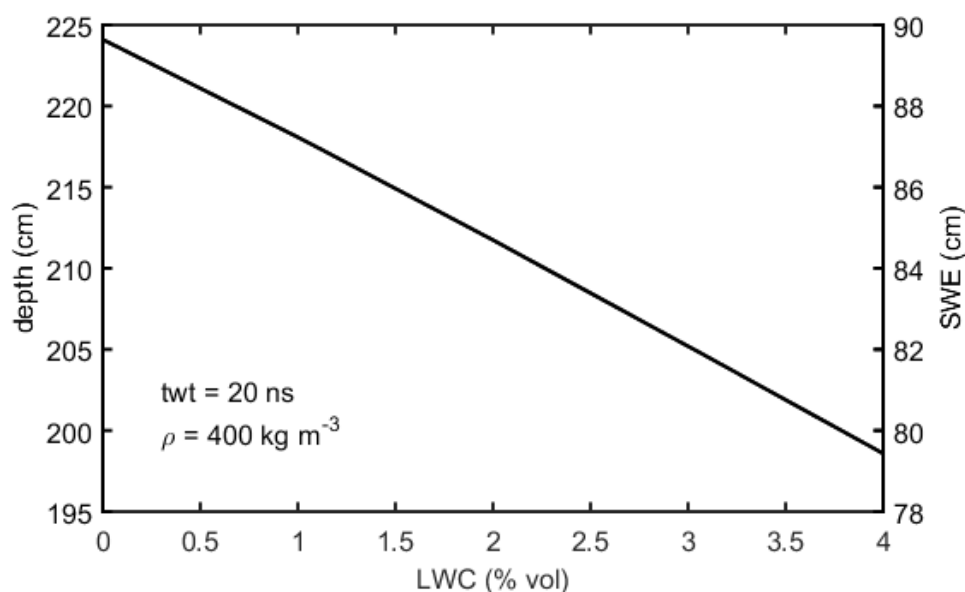


**Figure 17.** Change in depth and SWE as a result of LWC for a theoretical snow pack with 20ns two-way travel time and  $400 \text{ kg m}^{-3}$  density as a function of LWC.

The uncertainty of LWC values from tower-based measurements was determined by the variation in instantaneous frequency in the direct wave and ground surface reflection from snow-off conditions at the Banner Summit SNOTEL site between September 28 and October 2, 2016, during which time no precipitation was recorded at the SNOTEL precipitation gauge. The peak frequency of the ground surface reflection during this period was  $1190 \pm 70 \text{ MHz}$ . With the reference frequency taken to be the mean frequency, and downshift of 70MHz applied for a 2m snowpack, the resulting LWC

value is 0.25%, which is taken to be the uncertainty in the calculation due to system noise.

#### 4.2 Tower Mounted Sites

The network of continuously-running radars at tower mounted sites was evaluated directly over SNOTEL pillows at Bogus Basin (winters 2014/2015 and 2015/2016), Banner Summit (winter 2015/2016 and the Garden Mountain weather station precipitation gauges (winter 2015/2016). For the 2015/2016 winter the radars performed reliably at the Bogus Basin and Banner Summit SNOTELs and Garden Mountain weather station, with the few data gaps coming from relatively short periods of power loss which, once addressed, were not repeated. Data from the Vienna Mine SNOTEL, Fraser and Red Mountain Pass from the 2015/2016 winter were not collected in time to include in this thesis, but are expected to be continuous data sets.

For the following data sets radar traces were collected at 15 minute intervals and are compared to hourly SNOTEL values which have been interpolated to 15 minute intervals. Radar-derived SWE values were processed using the real-time algorithm described in Section 3.4. At the co-located SNOTEL locations, of which Bogus Basin and Banner Summit SNOTELs are presented, the ground surface reflection was difficult to distinguish from background noise levels for certain periods of time, owing to the presence of the bare ground, antifreeze pillow and tower base all within the field of view. All data presented was processed using the real-time algorithm, with up to several updated ground windows used as inputs to the algorithm for the Bogus Basin and Banner Summit SNOTEL sites. The Garden Mountain site, which was over bare ground and not an antifreeze pillow, did not require updated ground window inputs to the algorithm.

Changes to the updated ground windows could be reasonably expected in real-time measurement and transmission applications by monitoring the change in SWE. However, significant increases or decreases in SWE may require updated ground windows. Future versions of the automatic processing algorithm would likely be able to calculate these changes automatically and would not require user input. In all cases the reported radar-derived SWE values were calculated using the dry snow case, where the difference in two-way travel time between snow-off and snow-on ground reflections are used.

Since the dry snow case was applied with this processing, depth and density were not generally reported. During mid-winter cold periods, with dry snow, the snow surface is not continuously obvious in the radar reflection. LWC values are still obtained, since the surface reflection frequency is taken as the maximum instantaneous frequency across a full wavelength, approximately 20 samples. While a window to the expected surface reflection is not sufficient to get an accurate depth measurement, it is sufficient to be within a wavelength. Although the relevant updates to the radar firmware were not completed prior to this data collection, and no data was subsequently transmitted in real-time, data shown was the output of the automated real-time algorithm, and was capable of being transmitted via serial output and satellite modem. Although many studies have shown that snow pillows suffer their own error (e.g. Beaumont, 1965; Engeset et al., 2000), it is still the accepted continuous measurement of seasonal snow in the Western United States and forms a useful comparison to radar-derived values.

#### 4.2.1 Bogus Basin SNOTEL

Radar was installed at the Bogus Basin SNOTEL in November 2015, prior to first snowfall. A sustained cloudy period from mid-December, 2015, to early January, 2016,

resulted in power and data loss. After this failure, all battery banks were upgraded to 155amp-h or greater, and no further power losses occurred. Three other data gaps appear in the record, two in February and one in March. The gap in early February was the result of a firmware failure; the gaps in late February and mid-March were intentional removal of the radar system for firmware upgrades and testing. The last remaining data gap was the result of a bug in upgraded firmware, which was fixed at the next site visit.

Radar-derived SWE was processed with the automatic algorithm, and used three updated ground windows as inputs, corresponding to December 2, 2015, January 6, 2016 and January 15, 2016. The arm and mounted radar antenna were lowered from a height of 300cm to 255cm on January 6, which made the updated ground window on that date necessary. The purpose of lowering the arm was to attempt to decrease the amplitude of the reflection of the base of the tower in the radar antenna footprint, which was suspected of interfering with the ground surface reflection. A longer arm would have accomplished the same goal and would have been preferable; however, this would have resulted in the radar antenna being directly underneath the SNOTEL ultrasonic depth sensor and may have corrupted its measurements.

Radar-derived SWE was in good agreement with the SNOTEL SWE in the early season, prior to the mid-December data loss, and was subsequently well-correlated with SNOTEL SWE values once measurement began again in early January (Fig. 18). For the periods of measurement after early January the radar overestimated SWE as compared with the SNOTEL values by up to 12cm SWE, though the relative changes in SWE track well. The positive radar bias is consistent on a daily scale, and is therefore unlikely to be caused by underestimated liquid water, which would be more present during the warm

afternoon periods and result in an oscillating SWE value. The positive bias could be due to bridging, and under-measurement of SWE, by the SNOTEL pillow.

For the periods of coincident data collection after January 6, 2016, the percent error across all coincident measurements was  $-16 \pm 12\%$  (Fig. 19). Radar and SNOTEL SWE values were well-correlated during the period of coincident measurement, with a  $R^2$  value of 0.99 (Fig. 20). Although there was positive bias, the observations are highly correlated.

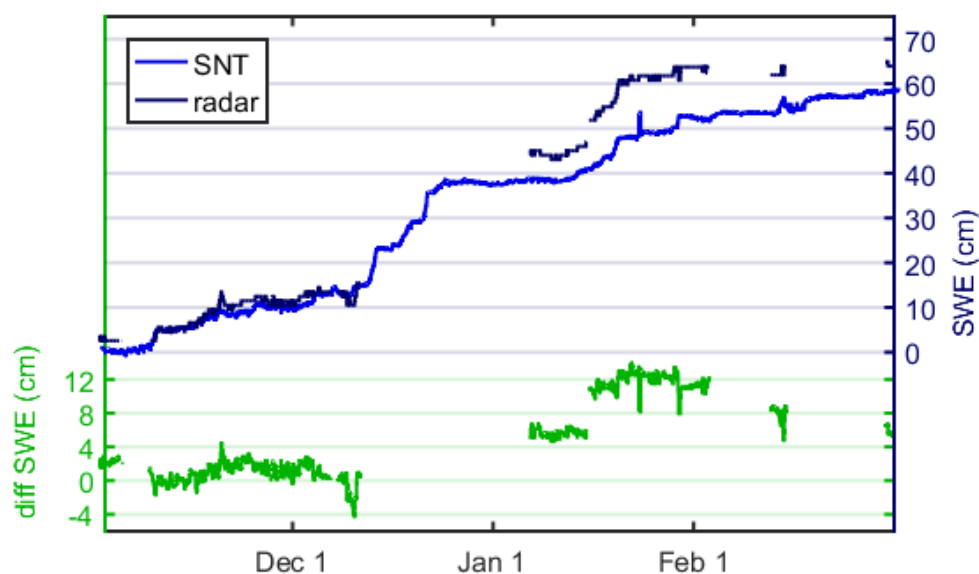


**Figure 18.** Radar (black) and SNOTEL (blue) SWE values, as well as the difference in SWE (green) for the Bogus Basin SNOTEL for the period November 1<sup>st</sup>, 2015 – March 1<sup>st</sup>, 2016. The radar-derived SWE output was from the automatic algorithm with three updated ground surface reflection windows on December 2, 2015, January 6, 2016 (coincident with lowering the antenna arm) and January 15, 2016. Several data gaps are present in this data set: the gap from mid-December to early January was the result of power loss; the gap in early February was the result of a firmware failure; and the gap in late February was intentional removal of the radar system for testing.

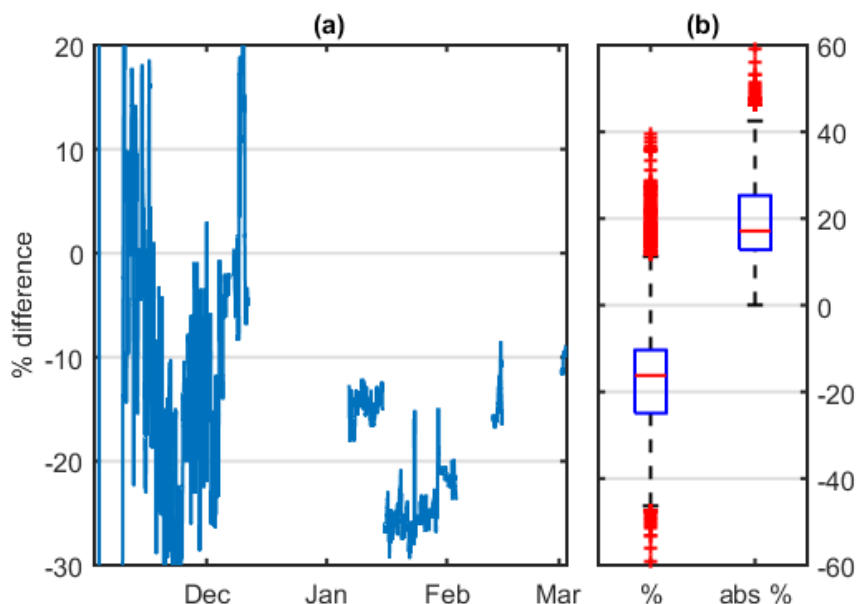


**Figure 19.** Percent error between radar-derived and Bogus Basin SNOTEL SWE values for the period of observation is shown in Subplot (a). The higher percent differences through mid-December correspond to relatively low differences in actual SWE amounts during the early season snow pack. Subplot (b) shows the total percent error of  $-16 \pm 12\%$  and absolute percent error of  $16 \pm 8\%$  for the period of observation.

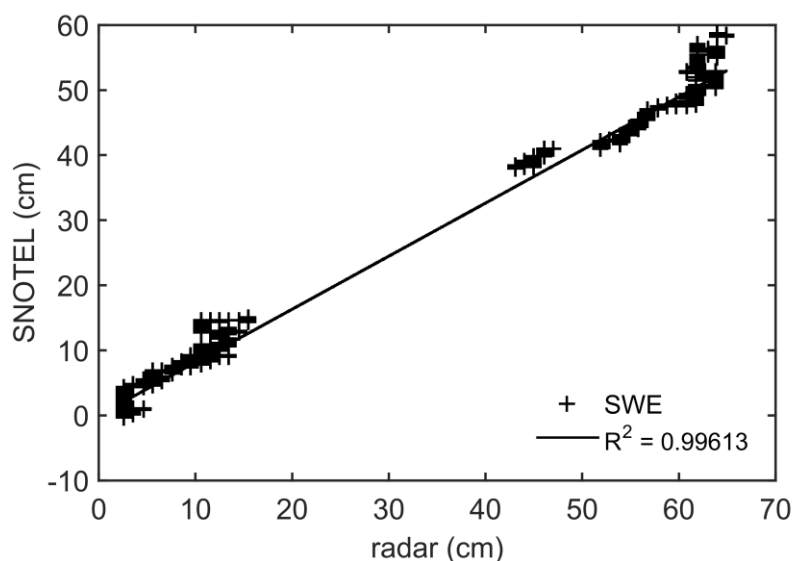


**Figure 20.** Correlation between radar-derived and SNOTEL SWE measurements at the Bogus Basin SNOTEL site, which have a  $R^2$  value of 0.99. Despite relatively high percent error between radar and SNOTEL SWE measurements, the two are highly correlated.

Radar-derived measurements of LWC at the Bogus Basin site were unreliable (Fig. 21). Although the radar produced LWC estimates that were physically reasonable during several above-freezing periods over the course of observation, there were also many sections of zero LWC during equally warm periods.

Although melt in the snowpack can be caused by radiation as well as temperature, and there is no available radiation data available for these sites, periods of above freezing temperatures are used as a qualitative proxy for expected melt, with temperatures taken from the SNOTEL. The correlation between temperature and LWC is used as an indicator for the reasonableness of the LWC values, and at the Bogus Basin site the temperature and LWC were not correlated at all (Fig. 22). Given the non-ideal placement of the antenna arm, which resulted in the base of the tower within the radar footprint, as well as the presence of the antifreeze pillow in the radar footprint, it seems reasonable that the ground surface reflection frequency was corrupted enough by other reflections that although the ground surface reflection could still be picked, the frequency was higher than it would have been without the additional reflection surfaces.

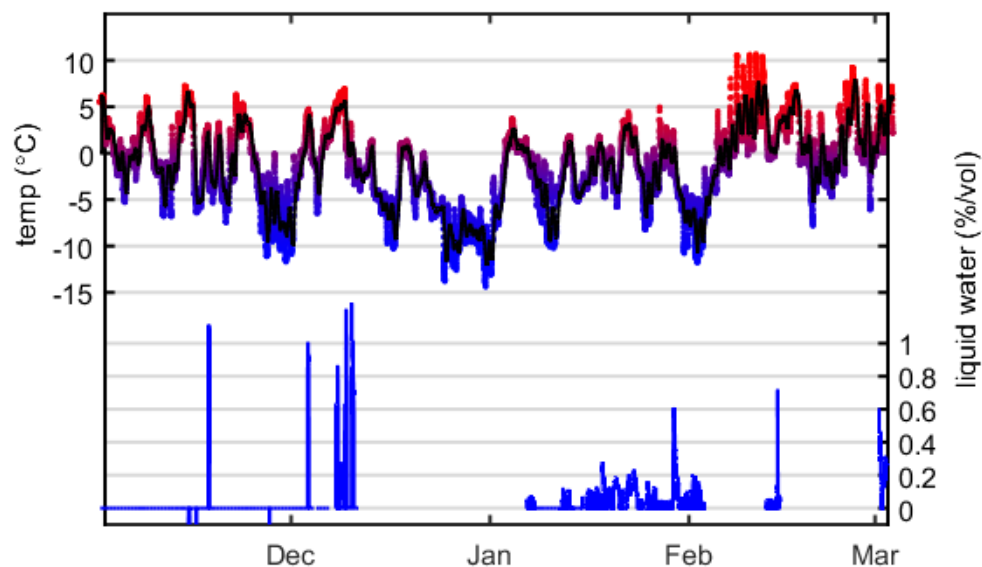


**Figure 21.** Bogus Basin SNOTEL temperature and radar-derived LWC. Temperature is color scaled, and the black line shows the daily mean temperature. Though the non-zero radar-derived LWC values are physical reasonable in isolation, and generally correspond with periods of above-freezing temperatures, there are large periods of time in which significant above-freezing temperatures do not result in non-zero LWC values.

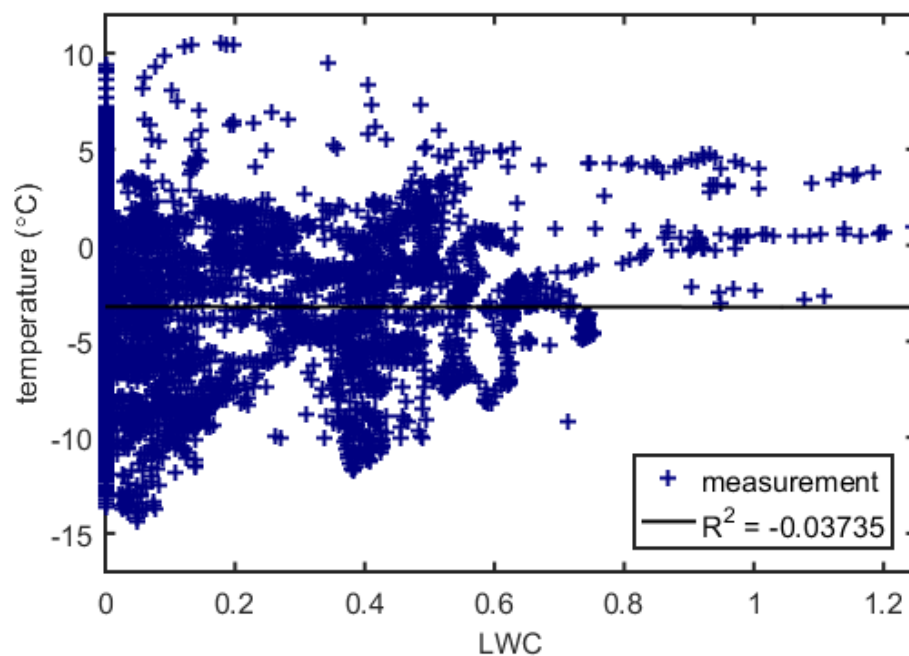


**Figure 22.** There is no correlation between radar-derived LWC and temperature at the Bogus Basin SNOTEL site for the observed period.

#### 4.2.2 Banner Summit SNOTEL

Radar was installed at the Banner Summit SNOTEL in mid-November, 2016. The original 100amp-h battery bank failed during a sustained cloudy period in mid-December, and during this power failure, a bug in the file system and loss of the on-board real time clock resulted in corrupted files. The site was visited in early January, and battery bank upgraded, which began the most comprehensive, continuous data set collected to-date. Continuous SWE measurements were made from January 14 through April 12, 2016, and covered a range in SWE values of 40-75cm as measured by the SNOTEL (Fig. 23).

Radar-derived SWE was processed with the automatic algorithm, and used three updated ground windows as inputs, corresponding to February 9, February 15 and March 4. The accumulation event from February 14-20 corresponded with the ground surface reflection being indistinguishable, which resulted in an unrealistic drop in SWE during that period. The radar recovered to reasonable values beginning on February 21. Several brief variations in SWE are obvious, up to  $\pm 6$ cm SWE in amplitude, which are the result of the automatic processing algorithm briefly picking an incorrect ground surface reflection. The algorithm quickly recovers, however. As with the Bogus Basin SNOTEL site, the radar overestimated SWE as compared with the SNOTEL values by up to 10cm SWE, though the relative changes in SWE track well. The positive radar bias is consistent on a daily scale, and is therefore unlikely to be caused by liquid water, which would be more present during the warm afternoon periods and result in an oscillating SWE value. The percent error across all coincident measurements was  $-9 \pm 5\%$  (Fig. 24). Radar and SNOTEL SWE values were well-correlated during the period of coincident measurement, with a  $R^2$  value of 0.94 (Fig. 25).

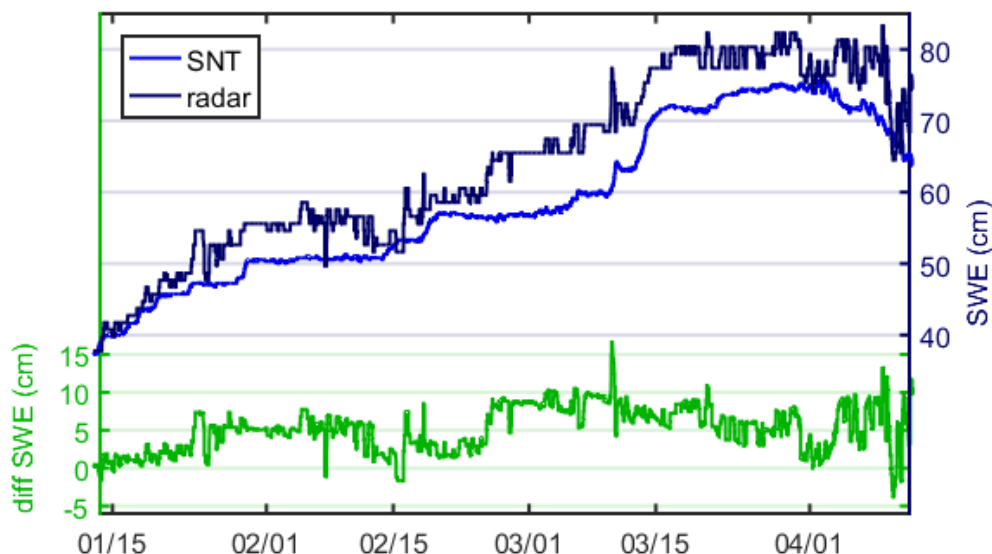


**Figure 23** Radar (black) and SNOTEL (blue) SWE values, as well as the difference in SWE (green) for the Banner Summit SNOTEL for the period January 12 – April 12, 2016, as processed by the automatic algorithm. The algorithm was updated at three points during the processing: February 9, February 15 and March 4, 2016. No filtering or other changes were applied to the algorithm outputs beyond the adjusted ground windows on those dates. The several sub-daily spikes in SWE, both positive and negative, correspond to places in which the automatic algorithm erroneously picked the ground surface, but soon recovered to the proper reflection target. The drop in radar SWE from February 14-16 is also erroneous, and represents a period in which the ground reflection was not obvious. After April 1, the ground surface also becomes difficult to pick and radar SWE values are increasingly variable. Note also that after the initial accumulation in mid-January the radar shows a strong positive bias in SWE. One possible explanation of this, which was also observed at the Bogus Basin SNOTEL, is that bridging of the SNOTEL pillow resulted in under-measurement of SWE. Radar-derived SWE is also stable on a daily scale, which suggests the high bias as compared to the SNOTEL values is not caused by daily spikes in LWC content, at least until mean daily temperatures remain below freezing prior to early April.

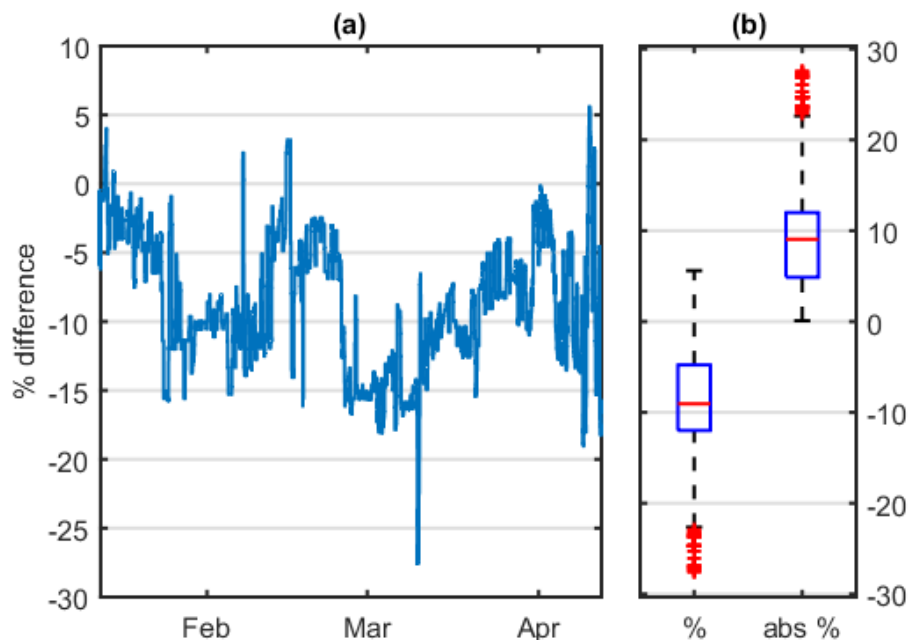


**Figure 24.** Percent error for radar-derived SWE as compared to Banner Summit SNOTEL values by date (a), as well as percent error of  $-9 \pm 5\%$  and absolute percent error for the full period of  $9 \pm 5\%$  (b).

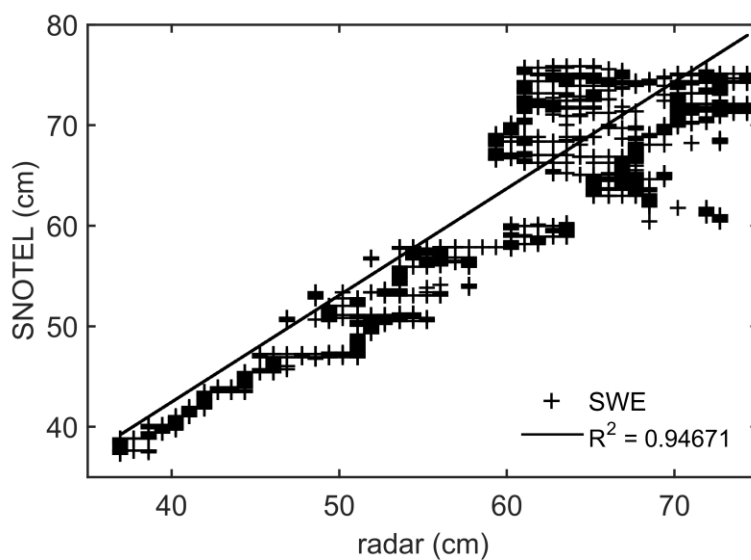


**Figure 25.** Correlation between radar-derived and SNOTEL SWE measurements at the Banner Summit site, which have a  $R^2$  value of 0.94.

Radar-derived LWC values at the Banner Summit SNOTEL site were again physically reasonable in terms of absolute values, but were much more consistent across measurements, compared with the Bogus Basin site. LWC values generally tracked with

daily mean temperatures, and ranged from 0-1.2% LWC (Fig. 26). There are many periods of expected LWC spikes on daily cycles during warm periods, as well as consistent non-zero LWC values responding to warm periods in late March and early April. The correlation between SNOTEL temperature and radar-derived LWC also suggested increased performance of the approach, with  $R^2$  value of 0.45 (Fig. 27).

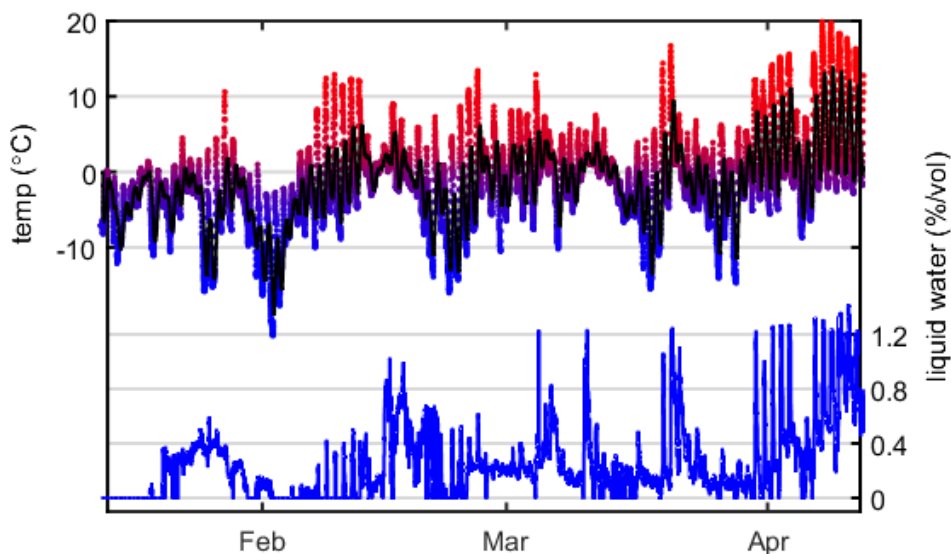


**Figure 26. Banner Summit SNOTEL temperature and radar-derived LWC. Temperature is color scaled, and the black line shows the daily mean temperature. LWC values respond well to above freezing temperatures on a daily-to-weekly scale. The issue of daily-scale zero values of LWC during periods of relatively warm temperatures, as observed at the Bogus Basin SNOTEL site, are not repeated at the Banner Summit SNOTEL site.**

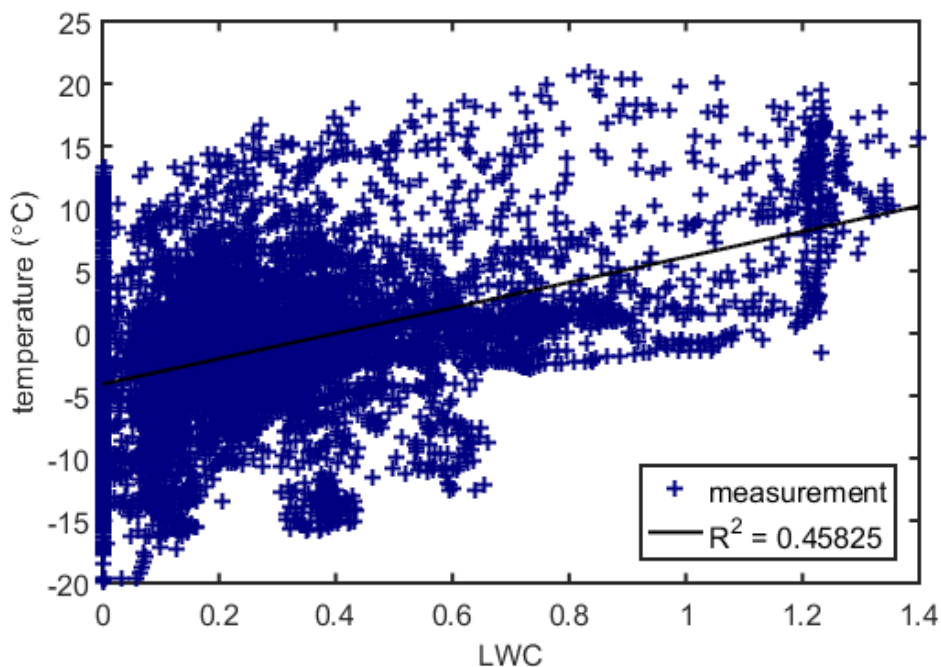


**Figure 27.** Correlation between Banner Summit SNOTEL temperature and radar-derived LWC has a  $R^2$  value of 0.45.

#### 4.2.3 Garden Mountain Weather Station

The Garden Mountain weather station does not have an independent measurement of SWE, such as a snow pillow, but does have a high-resolution precipitation gauge. The radar at the Garden Mountain site was installed above level ground, rather than a snow pillow as was the case at the SNOTEL sites. Wire mesh was secured to the ground surface below the radar prior to snowfall to enhance the ground surface reflection. The combination of the wire mesh on the bare ground surface, a longer mount arm (approximately 150cm) than was employed at either SNOTEL site, and lack of a pillow in the radar footprint, resulted in the ground reflection at this site being the most obvious and coherent of the three sites. The radar was in operation from December 16, 2015, to March 25, 2016 and radar-derived SWE from the site was again processed using the real-

time algorithm, and did not require an updated ground surface window, nor other user input.

Accumulated precipitation from the gauge values are shown starting November 1, 2015, and had at least one period of data loss in early February. In addition to the data gap, there was also nearly zero precipitation recorded during the second half of December, a period which saw significant accumulation in the radar data, as well as accumulation at SNOTEL sites such as Bogus Basin, suggesting some malfunction during this time. Radar-derived SWE values are reported along with the precipitation gauge measurement and an enhancement factor of 1.85 applied to the precipitation gauge, which matches recorded precipitation and SWE values for a known cold period in January (Fig. 28). Radar-derived SWE values were also highly correlated with precipitation gauge water equivalent measurements, with a  $R^2$  value of 0.94 (Fig. 29).

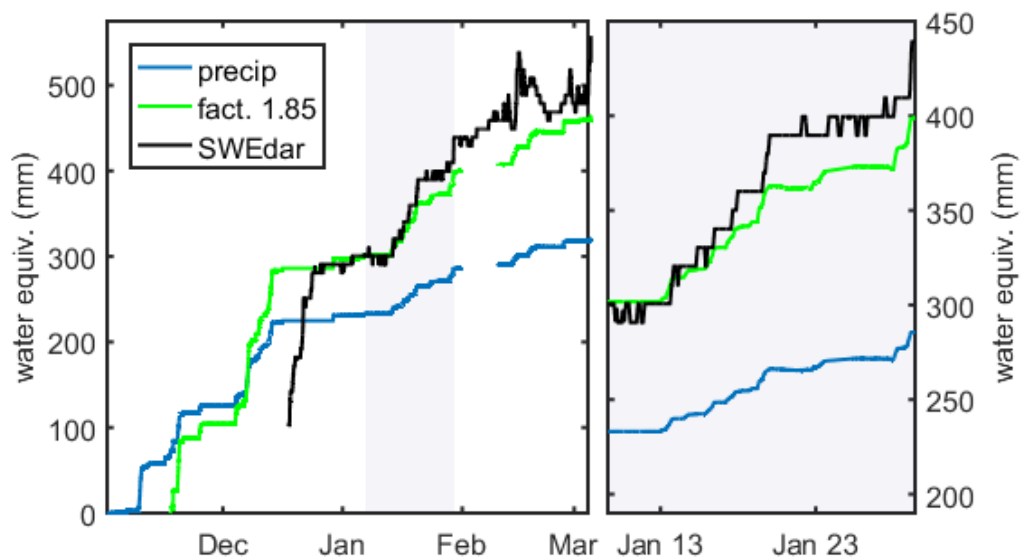


**Figure 28.** Precipitation gauge water equivalent (blue) and radar-derived SWE (black) for the Garden Mountain site. Also shown is a factor of 1.85 applied to the precipitation gauge value (green), which matches well with radar-derived SWE for the period with shaded background, January 7-30, 2016, when temperatures were cold and precipitation would have fallen as snow. Precipitation gauge measurements begin on November 1<sup>st</sup>, and the radar was installed on December 16<sup>th</sup>, 2015. The gap in precipitation gauge measurement corresponds to power loss at the gauge. Radar-derived SWE measurements are the output of the automatic algorithm, with no specific or updated ground surface window.

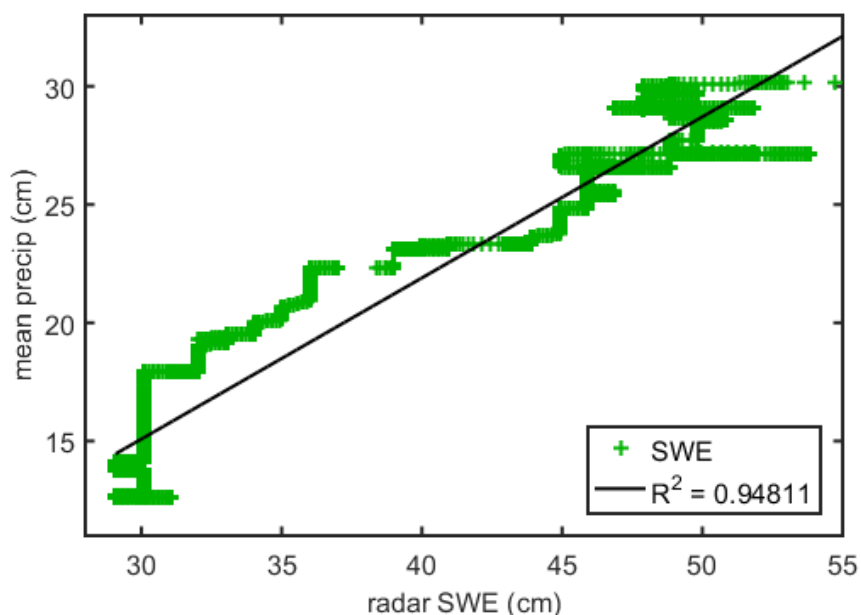


**Figure 29.** Correlation of precipitation gauge water equivalent and radar-derived SWE for the Garden Mountain site for periods of coincident measurement, with a  $R^2$  value of 0.94.

The radar and precipitation gauge are more correlated during cold periods with no melt but significant increases in SWE. For a four day period from January 16-20, there was a 6cm SWE accumulation event as measured by the radar (Fig. 30). During this cold period the radar and precipitation gauge were even more highly correlated, a  $R^2$  value of 0.97.

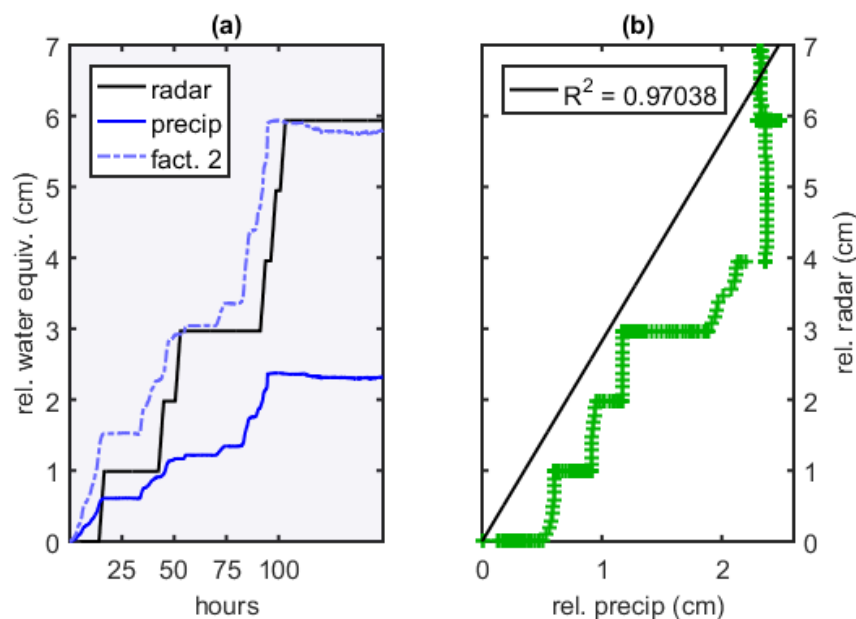


**Figure 30.** Correlation between radar-derived SWE and mean precipitation gauge at Garden Mountain, for the 100 hour period beginning January 3, 2016. Subplot (a) shows water equivalent from the radar (black), mean precipitation gauge (solid blue) and best fit factor of two applied to the mean precipitation (dashed blue), with values zeroed to the beginning of the period. The 7cm SWE event was highly correlated with  $R^2$  value of 0.97.

Radar-derived LWC measurements performed better compared to the Bogus Basin data set, similar to what was observed at Banner Summit (Fig. 31). In general, zero LWC values corresponded to periods of below-freezing mean daily temperatures. However, there was also a period of non-zero LWC in mid-January that is probably not physically reasonable, given that temperatures were consistently below freezing. A two week warm period February 9-21 resulted in moderate LWC values from 0.2-0.4%, although the uncertainty in LWC in both the Snow Fork and spectral shift method itself, in which the instantaneous frequency of the ground surface reflection varied by up to 100 MHz on an hourly basis during this period, is on the order of 0.5% LWC or greater. Radar-derived LWC then dropped again when below-freezing temperatures returned after

February 21. Temperature and LWC were reasonably correlated for the full period, with a  $R^2$  value of 0.42 (Fig. 32).

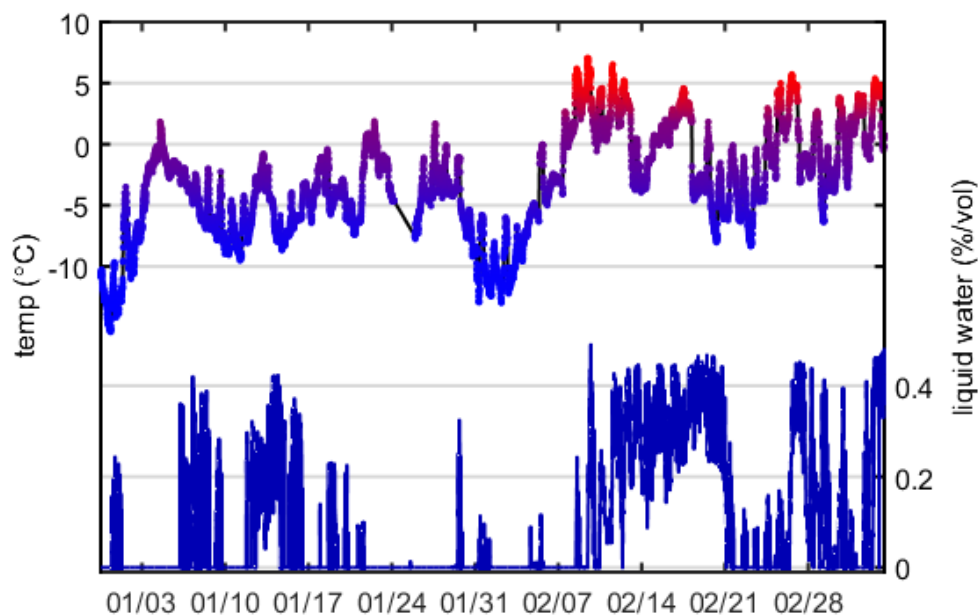


**Figure 31.** Garden Mountain temperature and radar-derived LWC. As with other tower-mounted sites there was not an independent measurement of LWC to compare to radar-derived values. However, the LWC signal generally appears to follow expected trends based on temperature data, especially the relatively spike in LWC follow a warm period in early February, and again in late February. Although daily temperature values drop below freezing between these warming events, the drop to zero LWC values between would seem to indicate an artifact of the processing, especially given non-zero LWC values in January.

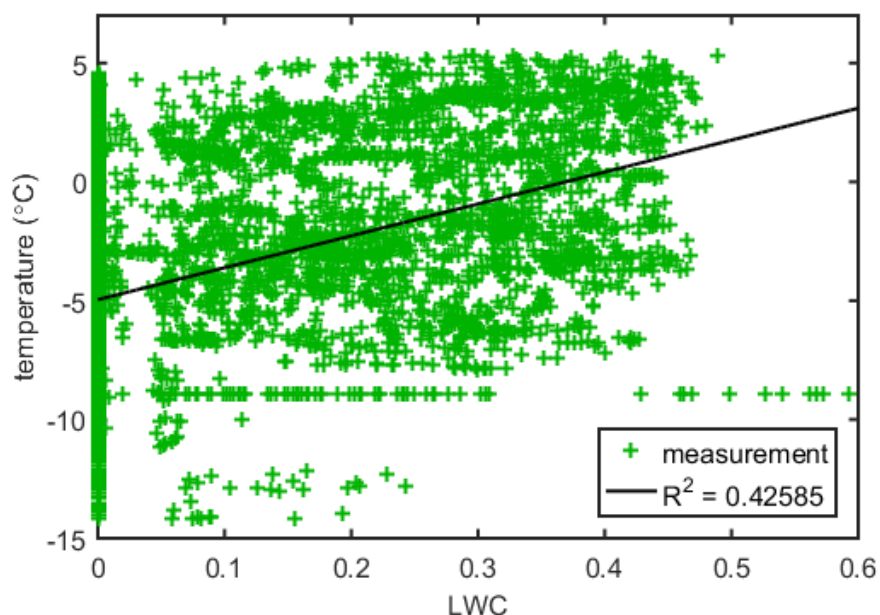


**Figure 32.** Correlation of temperature and LWC content at the Garden Mountain site, with a  $R^2$  value of 0.42.

## 5 Discussion

Tower-mounted impulse radar observations, combined with a new automated algorithm, produced consistent and well-correlated estimates of SWE as compared to both the standard remote measurement of SWE, the SNOTEL pillow, and a high-resolution precipitation gauge. At both the Bogus Basin and Banner Summit SNOTEL sites, the radar showed a consistent positive bias in SWE estimates after the initial accumulation period, which persisted through the winter season. Considering that bridging and underestimates of SWE by pillow sensors are a known phenomenon, this consistent bias in the radar SWE measurements is not concerning, and may in fact be a more accurate measure of SWE. Studies by researchers at Idaho Power have shown that this pillow records SWE values that are consistently less than SWE estimated from their high resolution precipitation gauge (Kunkel, personal communication, 2016).

Periods of power loss owing to insufficient battery storage with sub-150amp-h battery banks was an installation error and, while causing data gaps at every site, was corrected. The system hardware has performed well: as of the end of March, 2016, it has been deployed for approximately 1,500 unit-days, with one suspected antenna failure at the Garden Mountain site in mid-March, 2016, and one firmware update failure at the Bogus Basin SNOTEL site in February, 2016, which was corrected during the following site visit.

The radar performed the worst at the Bogus Basin SNOTEL site, which arose from the ground surface reflection being indistinguishable from other reflections for certain periods of time, caused in part by periods of mid-winter melt and rain. This site also had the shortest antenna arm mount, approximately 100cm, which led to the base of the tower being in the antenna footprint. Bare ground directly underneath the antenna, and the SNOTEL pillow itself were also in the radar footprint area. At each site the radar could have been mounted in a more ideal situation, with a longer mount arm; however, every effort was made to have the radar and SNOTEL measuring the same snowpack.

Now that the radar has been proven to be well correlated with the pillow measurements, future installations will not need to be constrained by a short mounting arm over the pillow, and can be moved so that the radar footprint is unobstructed. Although quantitative comparisons of footprint area and possible interference from the tower mount and pillow were not made between the Bogus Basin and Banner Summit sites, the Banner Summit radar did perform better in every measure, and also had fewer periods of undetermined ground surface reflection. At the Garden Mountain site, where the installation was much closer to the preferred arrangement and there were not

significant obstructions in the radar footprint, the ground surface reflection was always apparent in the radar data, and the automatic algorithm did not require any additional user input. Although the radar measurements could not be directly compared to an independent measurement of SWE at Garden Mountain, the radar SWE estimates were highly correlated with the precipitation gauge measurements for the cold winter periods. Further work needs to be done to accurately characterize the practical limits of the system in wet snow conditions.

The two most significant remaining hurdles that must be overcome, before the radar becomes a complete continuous, remote SWE sensor, are: 1) reliable automated snow surface detection, and 2) improvement and more validation of LWC estimates. In practice, the snow surface was only consistently identifiable by automatic detection for moderately warm periods, in which the surface layer was moderately wet and had a higher dielectric contrast as compared to dry, less dense snow. The result was that depth and density information were variable enough that they could not provide operational information. Since LWC was determined using the maximum instantaneous frequency of a wavelength at the reflection surface, the surface picking needed only to be within a wavelength, or approximately 10cm, of the actual surface. This was most often the case, and was likely not to be the cause of the second hurdle, which was the LWC calculations themselves. Future installations could include an independent measure of depth, such as high-frequency radar, laser range detection, or ultrasonic depth sensor, to obtain depth and density information, as well as give more confidence to the snow surface reflection frequency information. Both improvements, when completed, would give more accurate

estimates of SWE in wet snow conditions, when the difference in two-way travel time to the ground surface reflection is caused by liquid water in addition to snow.

Radar-derived LWC with this hardware and the spectral shift approach remains not well understood. Direct comparisons of the spectral shift approach in snow pits using the Snow Fork for independent verification yielded mixed results for moderate, >2% LWC. Some of this uncertainty could be explained by the majority of snow pits being dug on a slope, with Snow Fork measurements being taken up to several hours after the pit face was excavated. However, there is also not high confidence with radar-derived LWC values at the tower-mounted sites. Although there was not independent measurement of LWC at these sites, air temperature can be used as a proxy: periods of below-freezing temperatures will, in general, not see significant LWC, and periods with the daily mean temperature well above freezing should result in some LWC. Radar-derived LWC was completely uncorrelated with temperature at the Bogus Basin site, though in isolation the values produced were physically plausible. There were meaningful periods of time in which the ground surface reflection was identifiable, daily mean temperatures were well above freezing and the radar produced negligible LWC estimates. The Banner Summit and Garden Mountain sites performed better, with  $R^2$  values of 0.45 and 0.42, respectively. More detailed comparison with melt estimates from an energy balance model may help improve the understanding of the LWC retrieval accuracy.

## **6 Recommendations for Future Work**

Further work could improve both of accuracy of SWE estimates and the applicability of the sensor to a wider range of snowpack conditions. The physical mounting setup at the Bogus Basin and Banner Summit SNOTEL sites was non-ideal,

with the mounting arm extending the antenna a relatively short distance away from the tower. Future installations could be rotated away from the pillow itself, which would allow for a much longer mounting arm, reducing or eliminating the base of the tower from the radar footprint. This would result in significant improvement in the ground surface reflection signal at those sites. Since it has been demonstrated the radar and snow pillow estimates are highly correlated, it is no longer necessary to reduce the quality of the ground surface reflection by having the antenna directly over the pillow itself.

LWC estimates could be improved in several ways. Simply extending the mounting arm, as described above, would reduce reflections from the base of the tower, which could be responsible for artificial frequency responses in the instantaneous frequency that are not related to the snowpack. Development of a description of the attenuation of GPR signal for the frequencies above 1GHz, rather than applying the linear fit of the complex permittivity up to 1GHz, would be beneficial if errors introduced by the physical mounting are also addressed. Other methods of estimating LWC could also be explored, such as the use of independent depth information in combination with a mixing model approach (Mitterer et al., 2011).

Quantifying the accuracy of radar-derived SWE estimates for individual storm events, such as could be gathered by frequent site visits after storms and the use of storm boards, could also be useful.

In addition, improvements to SWE estimates in high LWC conditions could be made, even when the ground surface reflection is difficult to distinguish. The combination of independent depth information, such as an ultrasonic depth sensor, and a

SWE estimate using a density model, could be applied during periods when the ground surface reflection is not apparent.

## **7 Conclusion**

The technology and methods for remotely measuring SWE in the Western United States have not significantly changed since the inception of the NRCS SNOTEL network, in no small part because newer methods are either too expensive, not suitable for remote environments, or are unable to accurately measure SWE in a broad range of conditions. Radar in particular has been a promising tool for measuring SWE since the 1970's, but also has not seen wide-scale application beyond research environments because the required hardware has been expensive and not well-suited for remote sites, and processing the raw radar time domain measurements has required user input. This study demonstrates the viability of radar as an accurate remote SWE sensor through the creation and application of an automatic algorithm, which is capable of processing radar data on-site, which can then be transmitted. The algorithm was ported on new radar hardware, and compared well to the standard measure of remote SWE in the Western United States, the SNOTEL pillow, at two sites, as well as to a precipitation gauge at a third site. The algorithm is flexible enough to adapt to a range of tower-mounting heights and sites without undue site-specific calibration.

The central difficulty in processing the raw radar input was corrected with a temperature-dependent variation in the radar hardware sampling interval, which introduced large errors in SWE estimates when ignored. Empirical data from cold, dry periods at tower-mounted SNOTEL sites was used to create a temperature correction to the sample interval, and once a corrected sample interval was applied, left only a few

sample variation in ground surface reflection during periods of static SWE. The difference in travel time to the ground surface reflection in snow-off and snow-on conditions was used to directly estimate SWE using the assumption of dry snow. Although the snow surface reflection was often difficult to automatically identify in the algorithm, the difference in travel time to the ground was also used to create a window for the surface reflection when combined with a density approximation. Since the velocity of liquid water is much lower than that of ice, radar measurements of SWE in even moderately wet snow must account for the water, or suffer from significant under-measurement. The spectral shift method of calculating liquid water, based on the frequency-dependent attenuation of water in wet snow, was applied to do this. Once a wet snow SWE was also estimated, an error function could iterate as necessary to find the best possible surface reflection based on accepted limits to radar velocity in snow and snow density.

This algorithm was then applied with new hardware, which benefited greatly from a rugged design and which is capable of hands-off operation. The radar hardware is commercially unique in that it requires low enough power that it can be reliably operated with solar power in winter alpine environments. The on-board microprocessor is also robust, able to operate without user interaction for months at a time, and successfully rebooted and continued measurements after several periods of power loss.

The combination of hardware and automatic processing algorithm produced a SWE sensor which successfully operates in remote alpine environments. First, the radar was compared to a series of manual snow pit measurements of SWE to determine its accuracy, which is 7% SWE. Then, the radar was tower-mounted at a network of eight

sites. Three of those sites, the Bogus Basin SNOTEL, Banner Summit SNOTEL and Garden Mountain weather station, were operational for large portions of the 2016 winter season, and the radar-derived SWE could be compared to independent methods. At all three sites the radar was highly correlated with SNOTEL and precipitation gauge values, with  $R^2$  values of 0.94 or higher. Although the spectral shift method was incorporated to estimate SWE in wet snow conditions, LWC and ambient temperature were not well correlated. Even though melt in snow is driven by radiation as well as temperature, the lack of correlation with temperature suggest some error in the approach when used in combination with the physical radar installation at those locations. At the Bogus Basin and Banner Summit SNOTEL sites the antenna was mounted in a non-ideal location, with the antenna relatively close to the tower itself and the base of the tower within the field of view of the radar, which may have contributed to errors in LWC calculations there.

Despite higher uncertainty for wet snow conditions, the combination of a new automatic processing algorithm and field-appropriate hardware demonstrates that radar can be successfully used to measure SWE in remote environments.

## REFERENCES

- Annan, A., Cosway, S., Sigurdsson, T. 1994. GPR for snowpack water content. In Fifth International Conference on GPR. Waterloo, Ontario, Canada: Waterloo Centre for Groundwater Research, University of Waterloo, 465–475.
- Bales, R., Molotch, N., Painter, T., Dettinger, M., Rice, R., Dozier, J. 2006. Mountain hydrology of the western United States. *Water Resources Research*. 42, W08432.
- Barnett, T., Pierce, D., Hidalgo, H., Bonfils, C., Santer, B., Das, T., Bala, G., Wood, A., Nozawa, T., Mirin, A., Cayan, D., Dettinger, M. 2008. Human-induced changes in the hydrology of the western United States. *Science*. 319, 1080–1083.
- Beaumont, R., 1965. Mt. Hood pressure pillow snow gauge. *Journal of Applied Hydrometeorology*. 4, 626–631.
- Blöschl, G. 1999. Scaling issues in snow hydrology. *Hydrological Processes*. 13, 2149–2175.
- Bormann, K., Westra, S., Evans, J., McCabe, M. 2013. Spatial and temporal variability in seasonal snow density. *Journal of Hydrology*. 484, 63–73.
- Bradford, J. 2007. Frequency-dependent attenuation analysis of ground-penetrating radar. *Geophysics*. 72, J7–J16.
- Bradford, J., Harper, J., Brown, J. 2009. Complex dielectric permittivity measurements from ground-penetrating radar to estimate snow liquid water content in the pendular regime. *Water Resources Research*. 45, W08403.
- Cole, K., Cole, R. 1941. Dispersion and absorption in dielectric: I. Alternating current characteristics. *Journals of Chemical Physics*. 9, 341–351.
- Day, G. 1985. Extended streamflow forecasting using NWSRFS. *Journal of Water Resources Planning Management*. 111(2), 157–170.

- Deems, J., Fassnacht, S., Elder, K. 2006. Fractal distribution of snow depth from lidar data. *Journal of Hydrometeorology*. 7(2), 285-297.
- Denoth, A. 1994. An electronic device for long-term snow wetness recording. *Annals of Glaciology*. 19, 104–106.
- Dietz, A., Kuenzer, C., Gessner, U., Dech, S. 2012. Remote sensing of snow – a review of available methods. *International Journal of Remote Sensing*. 33(13), 4094 – 4134.
- Elder K., Rosenthal, W., Davis, R. 1998. Estimating the spatial distribution of snow water equivalence in a montane watershed. *Hydrologic Processes*. 12, 1793–808.
- Ellerbruch, D., Boyne, H. 1980. Snow stratigraphy and water equivalence measured with an active microwave system. *Journal of Glaciology*. 26, 225-233.
- Ellerbruch, D., Ellerbruch, D., Little, W., Boyne, H., Bachman, D. 1977. Microwave characteristics of snow. *Proceedings of the Western Snow Conference, 45th annual meeting*, 68-74.
- Engeset, R., Sorteberg, H., Udnaes, H. 2000. Snow pillows: use and verification. *Proceedings of the Fourth International Conference on Snow Engineering*. 2000, 45-51.
- Fierz, C., Fohn, P. 1994. Long-term observation of the water content of an Alpine snowpack. *Proceedings International Snow Science Workshop*. 1994, 117–131.
- Franz, K., Hogue, T., Sorooshian, S. 2008. Operational snow modeling: Addressing the challenges of an energy balance model for National Weather Service forecasts. *Journal of Hydrology*. 360, 48–66.
- Garen, D., Marks, D. 2005. Spatially distributed energy balance snowmelt modelling in a mountainous river basin: estimation of meteorological inputs and verification of model results. *Journal of Hydrology*. 315, 126-153.
- Georgakakos, K., Seo, D., Gupta, H., Schaake, J., Butts, M. 2004. Towards the characterization of streamflow simulation uncertainty through multimodel ensembles. *Journal of Hydrology*. 298, 222–241.

- Graves, D., Chang, H. 2007. Hydrological impacts of climate change in the Upper Clackamas River basin, Oregon, USA. *Climate Research*. 33, 143–157.
- Griffiths, D., 1989. *Introduction to electrodynamics*. Prentice Hall, Inc.
- Gubler, H., Hiller, M. 1984. The use of microwave FMCW radar in snow and avalanche research. *Cold Regions Science and Technology*. 9, 109-119.
- Hamlet, A., Lettenmaier, D. 2007. Effects of 20th century warming and climate variability on flood risk in the western US. *Water Resources Research*. 43, W06427.
- Heilig, A., Mitterer, C., Schmid, C., Wever, N., Schweizer, J., Marshall, HP, Eisen, O. 2015. Seasonal and diurnal cycles of liquid water in snow – measurements and modeling. *Geophysical Research Letters: Earth Surface*. 120(10), 2139-2154.
- Heilig, A., Schneebeli, M., Eisen, O. 2009, Upward-looking ground-penetrating radar for monitoring snowpack stratigraphy. *Cold Regions Science and Technology*. 59, 152-162.
- Johnson, J., Gelvin, A., Duvoy, P., Schaefer, G., Poole, G., Horton, G. 2015. Performance characteristics of a new electronic snow water equivalent sensor in different climates. *Hydrological Processes*. 29, 1418-1433.
- Jol, H. 2009. *Ground penetrating radar theory and applications*. Edited by H. Jol, *Ground Penetrating Radar Theory and Applications: Elsevier Science BV*.
- Jonas T., Marty, C., Magnusson, J. 2009. Estimating the snow water equivalent from snow depth measurements in the Swiss Alps. *Journal of Hydrology*. 378, 161–167.
- Kunkel, M., personal communication, 2016.
- Larson, K., Gutmann, E., Zavorotny, V., Braun, J., Williams, M., Nievinski, F. 2009. Can we measure snow depth with GPS receivers? *Geophysical Research Letters*. 36, L17502.

- Loukas, A., Vasiliades, L., Dalezios, N. 2002. Potential climate change impacts on flood producing mechanisms in southern British Columbia, Canada using the CGCMA1 simulation results. *Journal of Hydrology*. 259, 163–188.
- Luce, C., Holden, Z. 2009. Declining annual streamflow distributions in the Pacific Northwest United States, 1948–2006. *Geophysical Research Letters*, 36, 6-30.
- Lundberg, A., Thunehed, H. 2000. Snow wetness influence on impulse radar snow surveys theoretical and laboratory study. *Nordic Hydrology*. 31, 89-106.
- Marchand, W., Killingveit, A., Wilen, P., Wikstrom, P. 2003. Comparison of ground-based and airborne snow depth measurements with georadar systems, case study. *Nordic Hydrology*. 34, 427–448.
- Marks, D., Domingo, J., Susong, D., Link, T., Garen, D. 1999. A spatially distributed energy balance snowmelt model for application in mountain basins. *Hydrologic Processes*. 13, 1935-1959.
- Marshall, H.P., Koh, G., Forster, R. 2005. Estimating alpine snowpack properties using FMCW radar. *Annals of Glaciology*. 40, 157-162.
- Marshall, H.P., Koh, G. 2008. FMCW radars for snow research. *Cold Regions Science and Technology*. 52(2), 118-131
- Maurer, E. 2007. Uncertainty in hydrologic impacts of climate change in the Sierra Nevada, California, under two emissions scenarios. *Climatic Change*. 82, 309–325.
- McCreight, J., Small, E., Larson, K. 2014. Snow depth, density, and SWE estimates derived from GPS reflection data: Validation in the western U.S. *Water Resources Research*. 50(8), 6892-6909.
- Meløysund, V., Leira, B., Hoiseth, K., Liso, K. 2007. Predicting snow density using meteorological data. *Meteorological Applications*. 14, 413–23.
- Milly, P., Betancourt, J., Falkenmark, M., Hirsch, R., Kundzewicz, Z., Lettenmeier, D., Stouffer R.J. 2008. Stationarity is dead: whither water management? *Science*. 319, 573–574.

- Mitterer, C., Heilig, A., Schweizer, J., Eisen, O. 2011. Upward-looking ground-penetrating radar for measuring wet-snow properties. *Cold Regions Science and Technology*. 69, 129-138.
- Mizukami, N., Perica, S. 2008. Spatiotemporal variability of snowpack density in the mountainous regions of the Western United States. *Journal of Hydrometeorology*. 9, 1416–26.
- Molotch, N., Bales, R. 2005. Scaling snow observations from the point to the grid element: Implications for observation network design. *Water Resources Research*. 41, 0043-1397.
- Mote, P. 2003. Trends in snow water equivalent in the Pacific Northwest and their climate causes. *Geophysical Research Letters*. 30, 1601.
- Mote, P., Hamlet, A., Clark, M. Lettenmaier, D. 2005. Declining mountain snowpacks in western north America. *Bulletin of the American Meteorological Society*. 86 (1), 39–49.
- Offenbacher, E., Colbeck, S. 1991. Remote sensing of snow covers using the gamma-ray technique. USACE report.
- Okorn., R., Brunnhofer, G., Platzer, T., Heilig, A., Schmid, L., Mitterer, C., Schweizer, J., Eisen, O. 2014. Upward-looking L-band FMCW radar for snow cover monitoring. *Cold Regions Science and Technology*. 103, 31-40.
- Pagano, T., Garen, D., Sorooshian, S. 2004. Evaluation of official western U.S. seasonal water supply outlooks, 1922–2002. *Journal of Hydrometeorology*. 5, 896–909.
- Painter, T., Berisford, D., Boardman, J., Bormann, K., Deems, J., Gehrke, F., Hedrick, A., Joyce, M., Laidlaw, R., Marks, D., Mattman, C., McGurk, B., Ramirez, P., Richardson, M., Skiles, S., Seidel, F., Winstral, A. 2016. The airborne snow observatory: fusion of scanning lidar, imaging spectrometer, and physically-based modeling for mapping snow water equivalent and snow albedo. *Remote Sensing of Environment*. 184, 139-152.

- Proksch, M., Rutter, N., Fierz, C., Schneebeli, M. 2016. Intercomparison of snow density measurements: bias, precision and vertical resolution. *The Cryosphere*. 10, 371-384.
- Pulliainen, J. 2006. Mapping of snow water equivalent and snow depth in boreal and sub-arctic zones by assimilating space-borne microwave radiometer data and ground-based observations. *Remote Sensing of Environment*. 101, 257–269.
- Schmid, L., Heilig, A., Mitterer, C., Schweizer, J., Maurer, H., Okorn, R., Eisen, O. 2014. Continuous snowpack monitoring using upward-looking ground-penetrating radar technology. *Journal of Glaciology*. 60, 509-525.
- Serreze, M., Clark, M., Armstrong, R., McGinnis, D., Pulwarty, R. 1999, Characteristics of the western United State snowpack from snowpack telemetry (SNOTEL) data. *Water Resources Research*. 35, 2145-2160.
- Sihvola, A., Tiuri, M. 1986. Snow fork for field determination of the density and wetness profiles of a snow pack. *IEEE Transactions on Geoscience and Remote Sensing*. GE-24 (5), 717-721.
- Sturm, M., Holmgren, J., Liston, G. 1995. A seasonal snow cover classification system for local to global applications. *Journal of Climate*. 8, 1261–1283.
- Sturm, M., Taras, B., Liston, G., Derksen, C., Jonas, T., Lea, T. 2010. Estimating snow water equivalent using snow depth data and climate classes. *Journal of Hydrometeorology*. 11, 1380–94.
- Svomova, B. 2011. Winter climatic controls on spring snowpack density in the Western United States. *Arctic, Antarctic and Alpine Research*. 43, 118–26.
- Taner, M., Koehler, F., Sheriff, R. 1979. Complex seismic trace analysis. *Geophysics*. 44, 1041-1063.
- Techel, F., Pielmeier, C. 2011. Point observations of liquid water content in wet snow – investigating methodical, spatial and temporal aspects. *The Cryosphere*. 5, 405-418.

- Tiuri, M., Sihvola, A., Nyfors, E., Hallikaiken, M. 1984. The complex dielectric constant of snow at microwave frequencies. *IEEE Journal of Oceanic Engineering*. 5, 377-382.
- Trujillo, E., Ramirez, J., Elder, K. 2009. Scaling properties and spatial organization of snow depth fields in sub-alpine forest and alpine tundra. *Hydrological Processes*. 23(11), 1575-1590.
- Turner, G., Siggins, A. 1994. Constant Q attenuation of subsurface radar pulses. *Geophysics*. 59(8), 1192-1200.
- U.S. Soil Conservation Service: 1972, Hydrology, Sec. 4 of National Engineering Handbook, Soil Conservation Service, U.S. Department of Agriculture, Washington, D.C.
- Williams, C., McNamara, J., Chandler, D. 2009. Controls on the temporal and spatial variability of soil moisture in a mountainous landscape: the signature of snow and complex terrain. *Hydrological Earth Systems Science*. 13, 1325-1336.
- Wright, M., Kavanaugh, J., Labine, C. 2011. Performance Analysis of GMON3 Snow Water Equivalency Sensor. Proceedings of the 79th Annual Western Snow Conference, April 2011, Stateline, NV.

## APPENDIX

**Real Time Code**

```

% Real time SWE processing.
% MR 2016/8/16

%% INITIALIZE parameters, flags and options
close all;

% Just load this for testing...
load('');
rd.startDistance = zeros(size(rd.rawsignal(1,:)));

% These would be updateable buttons on UsbBuddy that are frequency used
rd.pauseTime      = 0;           % [s] pause between measurements
rd.vMin           = 1.8e8;       % [m/s] low limit for reasonable snow velocity in error
function
rd.vMax           = 2.6e8;       % [m/s] high limit for reasonable snow velocity in error
function
rd.rhoMin         = 0.22;        % [kg/m^3] low limit for reasonable snow density in error
function
rd.rhoMax         = 0.45;        % [kg/m^3] high limits for reasonable snow density in error
function
rd.iterLimit      = 20;          % max number of times to re-pick after initial error
rd.hm             = 2.7;         % [m] mounting height above ground
rd.surWinMin      = 40;          % [samples] number of samples to skip before minimum of
surface picking window
rd.gndUpdateMin   = 316;        % [samples] (min) Expected minimum location of ground
surface in raw signal. If
% this is set to anything besides 0 it will get used to set the
ground window
rd.gndUpdateMax   = 326;        % [samples] (max) Expected maximum location of ground
surface in raw signal.
rd.GWUnm          = 550;        % [integer] Number of measurements to use the
gndUpdateMin/gndUpdateMax settings
rd.GWUcounter     = 0;          % [number of iterations]
rd.depthEstDIMin  = 0;          % [m] (low) SWE value for application of depth estimate
rd.depthEstDIMax  = 0.350;      % [m] (high) SWE value for application of depth estimate
rd.depthEstScaleMin = 0.075;    % [kg m^3] (low) density value for depth estimate
rd.depthEstScaleMax = 0.25;     % [kg m^3] (high) density value for depth estimate
rd.dF             = 0.30;       % [%] +- depthEst factor (increase for larger surWindow size)
rd.nb             = 4*24*5;     % number of previous traces for background envelope
subtraction
rd.hWave          = 13;        % [samples] half wave to add back to time-zero

% These should be updateable, but these defaults will almost always work
rd.ampWindow      = 15;         % [samples] range of samples +- single pick to find peak
amplitude. Also gets used for
% finding the frequency of ground reflection
rd.surWindow      = 30;         % [samples] range of +- samples to get surface reflection
frequency
rd.frequencyWindow = 1;         % [samples] number of samples to average for
instantaneous frequency
rd.frequencyMethod = 'mean';    % min/mean/max for ground surface reflection (stick
with 'min' for now...)
rd.errorWindow    = 12;        % [traces] number of previous trace grd/surf pick to
consider for error
rd.pad            = 20;         % [samples] subtract from snow-off twt
rd.airSamps       = 0;          % [samples] 10/0
rd.airWindow      = 1:50;      % [samples] location of peak to flatten to for flatten2.m
function
rd.scaleFactor    = 1;          % [*] scaling factor (rd.fSwe = rd.dSwe*rd.scaleFactor +
rd.offset)
rd.offset         = 0;          % [+/-] offset factor (rd.fSwe = rd.dSwe*rd.scaleFactor +
rd.offset)
rd.gndMaxLim      = 450;

% Initialize some things, these don't need to be updated at all.
rd.vAir           = 2.99e8;     % [m/s] velocity in air
rd.vIce           = 1.68e8;     % [m/s] velocity in ice
rd.surPick        = [];         % initialize
rd.gndPick        = [];         % initialize
rd.gndOr          = [];         % initialize
rd.error          = [];         % initialize

```

```

%% Save directory
saveDir      = ' ';
fileName     = 'test.mat';

% Configuration settings
% config = returnDefaultSettings({10; 100; 1; 4; 250; 'Boost'; 6; []; []; '8mm'; [];
0});

% Would like to display these values as a double-check that the mounting
% height, settings and windows will work together
sv = showSettingValues(rd);

%% TAKE MEASUREMENT AND SAVE
runFlag      = 1; % Set to 1 for continuous run
error        = [0 0 0]; % measurement/calculation/iterLimit

nSigs        = length(rd.rawsignal(1,:));
numM         = 1; % number of measurements
en          = 500;
%%
for n = 1:nSigs
% while runFlag
% Take a measurement
% [signals, rd, errorMs] = realTimeMeasurement(rd,config,numM);
[signals, rd, errorMs] = realTimeMeasurementTEST(rd,numM);
error(1)        = errorMs;

% Calculate SWE if no error with measurement
if ~error(1)

    [rd,errorSWE,errorLim] = calculateSWE(signals,rd,numM);

    % Compile error flags
    error(2)        = errorSWE;
    error(3)        = errorLim;
    rd.error(numM,:) = error;

end

% Save
% save(fullfile(saveDir,fileName),'rd');

% Package for transmitting:
if errorSWE
    txData{1} = -1;
    txData{2} = -1;
    txData{3} = -1;
    txData{4} = -1;
    txData{5} = -1;
    txData{6} = -1;
    txData{7} = -1;
    txData{8} = -1;
    txData{9} = -1;
    txData{10} = -1;
    txData{11} = -1;
    txData{12} = signals;
else
    txData{1} = rd.date(numM);
    txData{2} = rd.dSwe(numM);
    txData{3} = rd.fSwe(numM);
    txData{4} = rd.gndPick(numM);
    txData{5} = rd.surPick(numM);
    txData{6} = rd.twt(numM);
    txData{7} = rd.depth(numM);
    txData{8} = rd.lwc(numM);
    txData{9} = rd.dt(numM);
    txData{10} = rd.temperature(numM);
    txData{11} = rd.error(numM,:);
    txData{12} = signals;
end

```

```
% Step the number of measurements taken  
numM = numM + 1;  
  
end
```

```

function [rd,errorSWE,errorLim] = calculateSWE(rawsignal,rd,nM)
% This function calculates SWE.
%
% INPUTS:  rawsignal = raw signal from from latest measurement...
%          rd = structure with containing settings, flags and
%             previous measurements
%          nM = number of measurements
%
% OUTPUTS: rd = structure with containing settings, flags and
%             previous measurements, updated to contain latest
%             measurement
%          errorSWE = error flag, [1] if error occurred during SWE
%                   calculation process
%          errorLim = error flag, [1] if processing iterated n >
%                   rd.iterLimit times and was timed out
% MR 2016/8/15

% Initialize a few things
errorSWE = 0;      % processing error
errorLim = 0;      % calculation hit iterLimit
checkVal = 1;     % Flag = 1 to send to error function
surFlag = 1;      % Flag = 1 for surface picking
zSFlag = 0;       % Flag = 1 to turn off error function and possible surface window re-
set
gndPick = [];     % initialize
surPick = [];     % initialize

% Make the SWE calculation, catch with error flag
try

    % Temperature correction
    dt = rtStepSizeCorrection(rd.temperature(nM));

    % A little processing...
    psignal = rawsignal;
    psignal = resample(psignal,dt);
    % All dts after using resample are now 'corrected' to what they would have been:
    % fullTwt = 27.28e-9 - therefor - dt = 27.28e-9/512 = 5.328e-11
    dt = 5.4e-11;
    % dt = 5.65e-11;

    % Flatten to direct wave peak and keep that 'lag'
    [psignal,lag] = flatten2(psignal,rd.airWindow);
    rd.env(:,nM) = hilbert(psignal);
    lag = lag + rd.airWindow(1) - 1;

    % We get a few weird ones...
    if lag < 0
        lag = 0;
    end

    [frequency,~] = InstantF(psignal,dt,rd.frequencyWindow); % instantaneous frequency
    psignal = normalize(psignal); % normalize direct wave to 1
    airTwt = (rd.hm - rd.startDistance(nM))*2/rd.vAir; % [s] snow-off twt to where
ground would be

    % The min/max reasonable samples to ground is:
    gndMin = round(airTwt/dt) - rd.pad - rd.hWave; % [samples] to snow-off
ground (this is the minimum - pad)
    depthMax = rd.hm - (rd.vAir*((rd.surWinMin + rd.hWave)*dt)/2);
    gndMax = round(depthMax*2/rd.vMin/dt);

    if gndMax > 512
        gndMax = 512;
    elseif gndMax > rd.gndMaxLim
        gndMax = rd.gndMaxLim;
    end

    % Get the gound window
    [rd,gndWindowMin,gndWindowMax] = setGndWindow(rd,gndMin,gndMax);

```

```

% Always calculate what the twt would be if the snow was dry to create a minimum
distance/window for picking the ground
% as well as to create window for surface picking
[gndPick,gndOr] = rtGrdPickEn(psignal,rd.gndOr(1:(nM-1)),gndWindowMin,gndWindowMax);
twtDiff        = (((gndPick + rd.hWave)*dt) - airTwt); % ADD BACK IN 1/2 WAVE!

minTwtDiff = 1e-20; % this sets the low limit at ~4cm SWE
if twtDiff < minTwtDiff
    twtDiff = 0;
end

% Depth of ice based only on difference in time to the ground
dIce = rd.vIce*twtDiff;

% Set the surWindowMin and surWindowMax values
[surWindowMin, surWindowMax, depthEst] = setSurWindow(rd,nM,gndPick,dIce);

% Tidy up any bad windows...
minPickDepth = 0.1; % [m] if estimated snow depth is less than this,
% won't attempt surface picking or
% error function
if abs(depthEst/2*dt*2.2e8) < minPickDepth;
    surFlag = 0; % turn off surface picking
    zSFlag = 1; % turn off error function
    surWindowMin = gndPick - depthEst;
    surWindowMax = gndPick - 1;

% If we end up with a bad surWindowMin or surWindowMax, revert to
% broadest limits...
elseif (surWindowMin < 1) || (surWindowMax > gndPick)
    surWindowMin = rd.surMinWin;
    surWindowMax = gndPick;
end

% Dry snow case SWE estimate
dSwe = dIce*0.917;

% Start the counter for number of iterations
iter = 1;
while checkVal == 1

    % Background subtraction of envelope if there are enough previous
    % traces to do so
    if nM > rd.nb
        bg = median(abs(rd.env(:,(nM - rd.nb):nM)),2);
        rd.backg(:,nM) = (abs(rd.env(:,nM)) - bg);
        rd.backg(:,nM) = rd.backg(:,nM)/max(rd.backg(:,nM));
    end

    % Pick the surface and make some estimate of the lwc. If values
    % error out the new surface window is given by the error function
    if iter <= rd.iterLimit;

        % Pick the surface
        if surFlag && nM > rd.nb
            surPick = rtSurfPickEn(rd.backg(:,nM),surWindowMin,surWindowMax);
        else
            surPick = gndPick - depthEst;
        end

        % Here's the processing
        twt = (gndPick - surPick)*dt;
        if twt > minTwtDiff

            depth = rd.hm - (rd.vAir*((surPick + rd.hWave)*dt)/2);
            [er,v] = BulkRealPermittivity(depth,twt);
            [fr,~] =
ReferenceFreq(gndPick,surPick,frequency,rd.surWindow,rd.frequencyMethod);
            [~,fg] =
ReferenceFreq(gndPick,surPick,frequency,rd.ampWindow,rd.frequencyMethod);
            [~,eis] = Qstar(twt,fr,fg,er);

```

```

% Scale to values at 1 GHz if necessary
if fr > 1e9
    [eis,~] = FScale(fr,eis);
end

lwc      = SnowLWC(eis,fg);
rho      = SnowDensity(er,lwc,fg);
swe      = rho*depth*0.917;

% If we are at low snow depths, skip most of this...
else
    twt      = 0;
    depth    = 0;
    [~,fg]   =
ReferenceFreq(gndPick,surPick,frequency,rd.ampWindow,rd.frequencyMethod);
    lwc      = 0;
    rho      = 0;
    swe      = 0;
    zSFlag   = 1;
    checkVal = 0;
end

% If we hit iterLimit, cut things off
elseif iter >= rd.iterLimit
    surPick  = -1;
    swe      = -1;
    errorLim = 1;

% Do we want to assign these though, if it iters out?
% Assign values
rd.rawsignal(:,nM) = rawsignal;
rd.psignal(:,nM)  = psignal;
rd.lag(nM)        = lag;
rd.airTwt(nM)     = airTwt;
rd.frequency(:,nM) = frequency;
rd.gndPick(nM)    = gndPick;
rd.gndOr(nM)      = gndOr;
rd.surPick(nM)    = surPick;
rd.twt(nM)        = twt;
rd.depth(nM)      = depth;
rd.lwc(nM)        = lwc;
rd.rho(nM)        = rho;
rd.swe(nM)        = swe;
rd.dSwe(nM)       = dSwe;
rd.fSwe(nM)       = dSwe*rd.scaleFactor + rd.offset;
rd.fr(nM)         = fr;
rd.fg(nM)         = fg;
rd.v(nM)          = v;
rd.dt(nM)         = dt;
rd.er(nM)         = er;
rd.eis(nM)        = eis;
rd.nIter(nM)      = iter - 1;

return

elseif surFlag == 0 % for no surface picking/low snow
    checkVal = 0;

    depth    = dIce/0.32;
    lwc      = 0.015;
    rho      = 0.32;
    swe      = rho*depth*0.917;

end

if ~zSFlag
    % Check it all out...
    [checkVal,newSurWindowMin,newSurWindowMax] = ...
rtFeError2(rd,v,rho,[rd.surPick(1:(nM-1)) surPick],surWindowMin,surWindowMax);
end

```

```

% If we error out, update the new surface window and lower the
% amp/noise threshold for a single peak pick
if checkVal == 1 && ~zSFlag
    surWindowMin = newSurWindowMin;
    surWindowMax = newSurWindowMax;
end

% Count how many times we try - limit while loop to iterLimit
iter      = iter + 1;
end

% Assign values
rd.rawsignal(:,nM) = rawsignal;
rd.psignal(:,nM)  = psignal;
rd.lag(nM)        = lag;
rd.airTwt(nM)     = airTwt;
rd.frequency(:,nM) = frequency;
rd.gndPick(nM)    = gndPick;
rd.gndOr(nM)      = gndOr;
if ~isempty(surPick)
    rd.surPick(nM) = surPick;
end
rd.twt(nM)        = twt;
rd.depth(nM)      = depth;
rd.lwc(nM)        = lwc;
rd.rho(nM)        = rho;
rd.swe(nM)        = swe;
rd.dSwe(nM)       = dSwe;
rd.fSwe(nM)       = dSwe*rd.scaleFactor + rd.offset;
% rd.fr(nM)       = fr;
% rd.fg(nM)       = fg;
% rd.v(nM)        = v;
rd.dt(nM)         = dt;
% rd.er(nM)       = er;
% rd.eis(nM)      = eis;
rd.surWindowMin(nM) = surWindowMin;
rd.surWindowMax(nM) = surWindowMax;
rd.depthEst(nM)    = depthEst;
rd.nIter(nM)      = iter - 1;

% If we error out in the calculation, set flag and return errors
catch

errorSWE          = 1;

% If we iter'ed out, these values probably still exist
try
rd.rawsignal(:,nM) = rawsignal;
rd.psignal(:,nM)  = psignal;
rd.lag(nM)        = lag;
rd.frequency(:,nM) = frequency;
rd.nIter(nM)      = nIter;
catch
rd.rawsignal(:,nM) = ones(512,1)*-1;
rd.psignal(:,nM)  = ones(512,1)*-1;
rd.lag(nM)        = -1;
rd.frequency(:,nM) = -1;
rd.nIter(nM)      = -1;
end

% Next, if we at least successfully made a gndPick, store that too
if ~isempty(gndPick)
    rd.gndPick(nM) = gndPick;
    rd.gndOr(nM)  = gndOr;
    rd.dSwe(nM)   = dSwe;
    rd.fSwe(nM)   = dSwe*rd.scaleFactor + rd.offset;
else
    rd.gndPick(nM) = -1;
    rd.gndOr(nM)  = -1;
    rd.dSwe(nM)   = -1;
end

```

```
end

% and these aren't as big of a deal if we don't store values
rd.airTwt(nM)    = -1;
rd.surPick(nM)  = -1;
rd.twt(nM)      = -1;
rd.depth(nM)    = -1;
rd.lwc(nM)      = -1;
rd.rho(nM)      = -1;
rd.swe(nM)      = -1;
% rd.fr(nM)     = -1;
% rd.fg(nM)     = -1;
rd.v(nM)        = -1;
rd.er(nM)       = -1;
rd.eis(nM)      = -1;

end
```